

## Exploring the mysterious high-ionization source powering [Ne V] in high- $z$ analog SBS0335-052 E with JWST/MIRI

MATILDE MINGOZZI,<sup>1</sup> MACARENA GARCIA DEL VALLE-ESPINOSA,<sup>2</sup> BETHAN L. JAMES,<sup>1</sup> RYAN J. RICKARDS VAUGHT,<sup>2</sup>  
MATTHEW HAYES,<sup>3</sup> RICARDO O. AMORÍN,<sup>4</sup> CLAUS LEITHERER,<sup>2</sup> ALESSANDRA ALOISI,<sup>2,5</sup> LESLIE HUNT,<sup>6</sup> DAVID LAW,<sup>2</sup>  
CHRIS RICHARDSON,<sup>7</sup> KARLA Z. ARELLANO-CÓRDOVA,<sup>8</sup> DANIELLE A. BERG,<sup>9</sup> JOHN CHISHOLM,<sup>9</sup> SVEA HERNANDEZ,<sup>1</sup>  
LOGAN JONES,<sup>2</sup> NIMISHA KUMARI,<sup>1</sup> CRYSTAL L. MARTIN,<sup>10</sup> SWARA RAVINDRANATH,<sup>11,12</sup> LIVIA VALLINI,<sup>13</sup> AND XINFENG XU<sup>14,15</sup>

<sup>1</sup>AURA for ESA, Space Telescope Science Institute, 3700 San Martin Drive, Baltimore, MD 21218, USA

<sup>2</sup>Space Telescope Science Institute, 3700 San Martin Drive, Baltimore, MD 21218, USA

<sup>3</sup>Stockholm University, Department of Astronomy and Oskar Klein Centre for Cosmoparticle Physics, AlbaNova University Centre, SE-10691, Stockholm, Sweden

<sup>4</sup>Instituto de Astrofísica de Andalucía (CSIC), Apartado 3004, 18080 Granada, Spain

<sup>5</sup>Astrophysics Division, Science Mission Directorate, NASA Headquarters, 300 E Street SW, Washington, DC 20546, USA

<sup>6</sup>INAF - Osservatorio Astrofisico di Arcetri, Largo E. Fermi 5, I-50125, Firenze, Italy

<sup>7</sup>Elon University, 100 Campus Drive, Elon, NC 27278, USA

<sup>8</sup>Institute for Astronomy, University of Edinburgh, Royal Observatory, Edinburgh EH9 3HJ, UK

<sup>9</sup>Department of Astronomy, The University of Texas at Austin, 2515 Speedway, Stop C1400, Austin, TX 78712, USA

<sup>10</sup>Department of Physics, University of California, Santa Barbara, Santa Barbara, CA 93106, USA

<sup>11</sup>Astrophysics Science Division, NASA Goddard Space Flight Center, 8800 Greenbelt Road, Greenbelt, MD 20771, USA

<sup>12</sup>Center for Research and Exploration in Space Science and Technology II, Department of Physics, Catholic University of America, 620 Michigan Ave N.E., Washington DC 20064, USA

<sup>13</sup>INAF – Osservatorio di Astrofisica e Scienza dello Spazio di Bologna, Via Piero Gobetti, 93/3, I-40129 Bologna, Italy

<sup>14</sup>Department of Physics and Astronomy, Northwestern University, 2145 Sheridan Road, Evanston, IL 60208, USA

<sup>15</sup>Center for Interdisciplinary Exploration and Research in Astrophysics (CIERA), Northwestern University, 1800 Sherman Avenue, Evanston, IL 60201, USA

(Received ; Revised ; Accepted)

Submitted to ApJ

### ABSTRACT

Nearby blue compact dwarf galaxies (BCDs) share similar properties with objects from the Epoch of Reionization revealed by JWST, in terms of low stellar mass, low metallicity and high specific star-formation rate. Thus, they represent ideal local laboratories for detailed multi-wavelength studies to understand their properties and the mechanisms shaping them. We report the first JWST MIRI/MRS observations of the BCD SBS 0335-052 E, analyzing MIR emission lines tracing different levels of ionization (e.g., [Ne II], [S IV], [Ne III], [O IV], [Ne V]) of the ionized gas. SBS 0335-052 E MIR emission is characterized by a bright point source, located in one of the youngest and most embedded stellar clusters ( $t \sim 3$  Myr,  $A_V \sim 20$ ), and underlying extended high-ionization emission (i.e., [O IV], [Ne V]) from the surroundings of the older and less dusty stellar clusters ( $t < 20$  Myr,  $A_V \sim 8$ ). From the comparison with state-of-the-art models, we can exclude shocks, X-ray binaries, and old stellar populations as the main sources of the high ionization. Interestingly, a 4-16% contribution of a  $\sim 10^5 M_\odot$  intermediate massive black hole (IMBH) is needed to justify the strong [Ne V]/[Ne II] and would be consistent with optical/UV line ratios from previous studies. However, even IMBH models cannot explain the strongest [O IV]/[Ne III]. Also, star-forming models (regardless of including X-ray binaries) struggle to reproduce even the lower ionization line ratios (e.g., [S IV]/[Ne II]) typically observed in BCDs. Overall, while current models suggest the need to account for an accreting IMBH in this high- $z$  analog, limitations still exist in predicting high-ionization emission lines (I.P.  $> 54$  eV) when modeling these low-metallicity environments, thus other sources of ionization cannot be fully ruled out.

*Keywords:* Blue compact dwarf galaxies (165), Infrared spectroscopy (2285), Emission line galaxies (459), Interstellar medium (847), Intermediate-mass black holes (816), High-redshift galaxies (734)

## 1. INTRODUCTION

In the JWST era, surveys such as the *JWST Advanced Deep Survey* (JADES), the *Cosmic Evolution Early Release Science Survey* (CEERS) and the *Ultradeep NIRSpect and NIRCcam Observations before the Epoch of Reionization* (UNCOVER) have started to revolutionize our knowledge of the early Universe up to  $z \sim 14$  (e.g., Bagley et al. 2023; Bunker et al. 2023; Bezanson et al. 2024; Carniani et al. 2024a), exploring the epoch of reionization (EoR,  $z > 6$ ) as never done before. Several studies over the past decade have suggested that low-mass, metal-poor and highly star-forming galaxies can play a crucial role in the EoR (e.g., Wise et al. 2014; Robertson et al. 2015; Stark et al. 2015), as now supported by recent JWST works probing the details of ultra-faint galaxies (e.g., Atek et al. 2024; Simmonds et al. 2024). JWST has also started to reveal an unprecedented number of active galactic nuclei (AGN) in the first billion years, comprising both intrinsically faint and reddened sources (e.g., Harikane et al. 2023; Maiolino et al. 2023a; Labbé et al. 2023; Kocevski et al. 2024; Übler et al. 2024; Juodvzbalis et al. 2024), including a new family of objects, the so-called Little Red Dots (e.g., Furtak et al. 2023; Kokorev et al. 2024; Matthee et al. 2024). The role that these AGN can play in the EoR is currently under investigation (e.g., Dayal et al. 2024), but it is still challenging to unambiguously identify AGN activity in EoR systems.

To detect the presence of faint AGN at  $4 < z < 12$ , many works used the detection of broadened Balmer lines (FWHM  $\sim 1000 - 5000$  km/s; e.g., Harikane et al. 2023; Maiolino et al. 2023a; Larson et al. 2023; Kokorev et al. 2023; Greene et al. 2024; Greene & Ho 2004). However, the broad component under forbidden lines can simply be too faint to be detected (e.g., Carniani et al. 2024b), leading to possible mis-classification of a pure star-forming system with a fast gas outflow as a broad line AGN. AGN classification has been also proposed via the presence of high-ionization rest-UV and blue optical lines (e.g., N IV]  $\lambda\lambda 1483, 7$ , [N III]  $\lambda 1750$ , C IV  $\lambda\lambda 1548, 51$ , [Ne IV]  $\lambda 2423$ , He II  $\lambda 4686$ ; Maiolino et al. 2023b; Kokorev et al. 2024; Greene et al. 2024; Backhaus et al. 2024). However, optical and UV diagnostics can be less effective in metal-poor systems (e.g., Feltre et al. 2016; Übler et al. 2023), because a hard stellar radiation field and AGN activity can behave similarly in low-metallicity dense environments (e.g., Leitherer et al. 1999; Eldridge et al. 2017; Telford et al. 2023). Thus, metal-poor star-forming systems can show UV and optical high-ionization lines similar to those observed in high- $z$  AGN candidates (e.g., the star-forming RXCJ2248-ID at  $z \sim 6$ ,

Topping et al. 2024), making the two scenarios difficult to distinguish (e.g., Castellano et al. 2024; Álvarez-Márquez et al. 2024). Another proposed method to identify AGN is through photometric variability resulting from changes in AGN mass accretion rate (Hayes et al. 2024), but larger samples of AGN at high- $z$  are needed to reduce the statistical and systematic uncertainties.

In this context, nearby galaxies can provide a precious opportunity for us to understand the characteristics of the interstellar medium (ISM) of these primeval objects and how to distinguish between star-formation and AGN activity within them, given the high signal-to-noise (S/N) of their spectra and the possibility to perform spatially resolved and multi-wavelength studies. In particular, nearby blue compact dwarf galaxies (BCDs) are ideal analogs to these high- $z$  systems, as they share properties in terms of stellar mass, intense star formation activity and metal poor content, as also suggested by recent JWST studies (e.g., Schaerer et al. 2022; Brinchmann 2023). Many studies have explored these objects to understand how to constrain their ISM properties using their optical and UV emission (e.g., James et al. 2009; Izotov et al. 2012; Berg et al. 2019; 2021; Senchyna et al. 2021; 2023; Mingozi et al. 2022; 2024; Kumari et al. 2024). In this context, the mid-infrared (MIR) wavelength range covers a large range of ionization potentials for the same species (e.g., 20-126 eV, [Ne II]  $\lambda 21.56\mu\text{m}$ , [Ne III]  $\lambda 15.56\mu\text{m}$ , [Ne V]  $\lambda\lambda 14.32, 24.3\mu\text{m}$ , [Ne VI]  $\lambda 7.65$ ) at lower excitation energies. While these lines are not accessible in the high- $z$  universe, they can provide an important constraint on the gas ionization mechanisms and, by also probing other phases (i.e., warm molecular gas with  $\text{H}_2$  rotational lines; dust with polycyclic aromatic hydrocarbons, PAHs), they can give a broad overview of the ISM conditions.

In this work, we focus on the galaxy SBS 0335-052 E ( $z \sim 0.01352$ ;  $1'' \sim 280$  pc), discovered by Izotov et al. (1990). This object is a nearby BCD, extremely metal-poor ( $\sim 5\% Z_{\odot}$ ;  $12 + \log(\text{O}/\text{H}) \sim 7.2 - 7.3$ ; Papaderos et al. 2006) and characterized by a compact vigorous starburst (specific star formation rate,  $\log(sSFR/\text{Gyr}^{-1}) \sim -8.13$ ; Rémy-Ruyer et al. 2015) and massive young clusters (Papaderos et al. 1998; Reines et al. 2008; Adamo et al. 2010 and references therein). This galaxy is also well-known for a complex kinematics and a large scale  $\text{H}\alpha$  outflow (Herenz et al. 2023) and high-ionization optical and UV emission lines typically observed in the EoR (e.g., He II  $\lambda 4686$ , C IV  $\lambda\lambda 1548, 51$ , He II  $\lambda 1640$ ; Herenz et al. 2017; Kehrig et al. 2018; Wofford et al. 2021). In particular, its extended nebular He II  $\lambda 4686$  emission requires energy beyond 54.4 eV (i.e.,  $> 4$  Ryd,

$\lambda < 228 \text{ \AA}$ ), indicative of a very hard ionizing spectral energy distribution (SED), that only rotating metal-free or extremely metal-poor massive stars seem capable of reproducing (Kehrig et al. 2018; see also Wofford et al. 2021). Recent studies have also suggested that SBS 0335-052 E may host an intermediate massive black hole (IMBH) of  $\sim 10^3 - 10^5 M_{\odot}$  to explain its [Ne V]  $\lambda 3426$  emission (Hatano et al. 2024, see also Thuan & Izotov 2005), requiring energies beyond 97 eV (i.e.,  $> 7.1 \text{ Ryd}$ ,  $\lambda < 128 \text{ \AA}$ ), as well as possible near IR variability (Hatano et al. 2023). IMBHs (see Greene et al. 2020 for a review) could represent the missing piece between stellar and supermassive BHs and would help explain the rapid accretion processes in place at high- $z$ . Thus, it is important to understand if galaxies such as SBS 0335-052 E can host an accreting IMBH, and, if so, which are the best diagnostics to trace its activity and impact on the ISM.

To this end, we exploit JWST/MIRI Medium Resolution Spectroscopy (MRS) integral field spectroscopy (IFS) data to investigate the possible accreting IMBH or other non-stellar source ionizing the high- $z$  analog SBS 0335-052 E's ISM, using spatially resolved high ionization MIR lines. Indeed, SBS 0335-052 E intense SF activity makes this galaxy particularly bright in the MIR, which represents  $\sim 75\%$  of its total luminosity (Plante & Sauvage 2002). Spitzer IRS 5.3–35  $\mu\text{m}$  spectrum already revealed strong MIR emission lines (i.e., [S IV]  $\lambda 10.51$ , [Ne III]  $\lambda 15.55$ , [O IV]  $\lambda 25.89$ ), warm molecular gas features (i.e.,  $\text{H}_2 0-0 \text{ S}(3)$ ) and the absence of PAHs (Houck et al. 2004; Hao et al. 2009). Nevertheless, MIRI/MRS offer the considerable advantage of spatially resolving the MIR emission (down to  $\sim 0.4-0.9''$ ,  $\sim 112-252 \text{ pc}$ ) and thus revealing the location of very high ionization extended emission (i.e., [Ne V]  $\lambda 14.32 \mu\text{m}$ ) for the first time in BCDs.

In Sec. 2, we present the observations and data reduction. In Sec. 3, we show the methods we adopted for our data analysis, including spectral fitting and literature photoionization and shock models that we used to interpret our results, reported in Sec. 4. In Sec. 5, we discuss our findings as well as possible limitations in current models, while in Sec. 6, we conclude with a summary of our work. Throughout this work we assume a flat  $\Lambda\text{CDM}$  cosmology ( $H_0 = 70 \text{ km/s/Mpc}$ ,  $\Omega = 0.3$ ) and  $12+\log(\text{O}/\text{H})_{\odot} = 8.69$  (Asplund et al. 2009).

## 2. OBSERVATIONS AND DATA REDUCTION

SBS 0335-052 E data were acquired as part of the Cycle 2 JWST program PID 4278 (PI: Mingozi) on February 11, 2024. In particular, the galaxy was observed with JWST/MIRI MRS using the three MRS grating settings (SHORT, MEDIUM, and LONG;  $\lambda \sim 5-28 \mu\text{m}$ ), and the FAST readout mode. Just one pointing was used since MIRI/MRS covers the majority of SBS 0335-052 E's active starburst activity with Channel 1 ( $3.2'' \times 3.7''$ ) and fully

samples it in Channel 4 ( $6.6'' \times 7.7''$ ). Given the JWST pointing accuracy of  $\sim 0.1''$ , target acquisition was not required. A 4-point dither pattern was also applied to achieve optimal sampling throughout the MRS field of view (FOV) and to identify and remove detector artefacts. Each pointing was observed with 50 groups per integration for a total on-source exposure time of 1665 s. Dedicated background observations were performed with half the integrations (same group number but half the dithering) to accurately measure and correct for the thermal background. Background and science observations were connected via a fixed offset and placed in an uninterrupted sequence, and a PA orientation range was required to obtain simultaneous imaging observations using the F770W, F1130W, and F1800W filters, which will be presented in a forthcoming paper.

We retrieved MIRI/MRS raw products from Mikulski Archive for Space Telescopes (MAST) and we processed the data with v1.16.0 of the JWST calibration pipeline, following the `jupyter notebook` provided by the MIRI team. As extra steps to the standard version of the MIRI pipeline, we masked additional regions affected by cosmic showers at the end of Stage 1 (`ShowerMasking Notebook`) and we applied residual fringe corrections in Stage 2. We subtracted the background in Stage 3, using the master background created by the pipeline. In Stage 3 we created the final datacubes per band, to optimize the fringing correction, obtaining 12 datacubes centered to the same coordinates and keeping the native pixel scale size (i.e.,  $0.13''$ ,  $0.17''$ ,  $0.20''$  and  $0.35''$ , for Channel 1, 2, 3 and 4, respectively). Nevertheless, we note that few spaxels located at the peak of the MIR emission are still affected by significant fringing, especially in Channels 3 and 4. The FOV progressively increases from  $3.2'' \times 3.7''$  in Channel 1, to  $6.6'' \times 7.7''$  in Channel 4, as well as the MIRI/MRS PSF and spatial resolution, from  $\sim 0.4''$  in Channel 1 to  $\sim 0.9''$  in Channel 4.

In Fig. 1 we show the position of MIRI/MRS FOV superimposed on the HST ACS F150LP UV emission (left panel) and the 12-17  $\mu\text{m}$  slice from MIRI/MRS Channel 3 (right panel). The UV emission (map and grey contours) clearly shows the six young, massive and compact “super star clusters” (SSC1, SSC2, SSC3, SSC4, SSC5, SSC6) revealed in this galaxy (Thuan et al. 1997). SSCs1-6 clusters have ages and masses in the range  $\sim 3-15 \text{ Myr}$  and  $\sim 3-30 \times 10^5 M_{\odot}$  (Reines et al. 2008; Adamo et al. 2010; see also Tab. 2), and luminosity of  $\sim 10^8 L_{\odot}$ , all within  $\sim 2'' \sim 500 \text{ pc}$  (Thuan et al. 1997). One of them, SSC1, is also known for its enhanced obscuration (Hunt et al. 2001). The He II  $\lambda 4686$  high-ionization emission revealed with MUSE (white dotted contours; seeing  $\sim 0.7-0.8''$ ) follows the UV emission and peaks around SSCs4,5. The HST  $\text{H}\alpha$  black dashed contours highlight the three additional actively young star-forming regions, S3-Pa $\alpha$ , S7 and S8, discovered by Thompson et al.

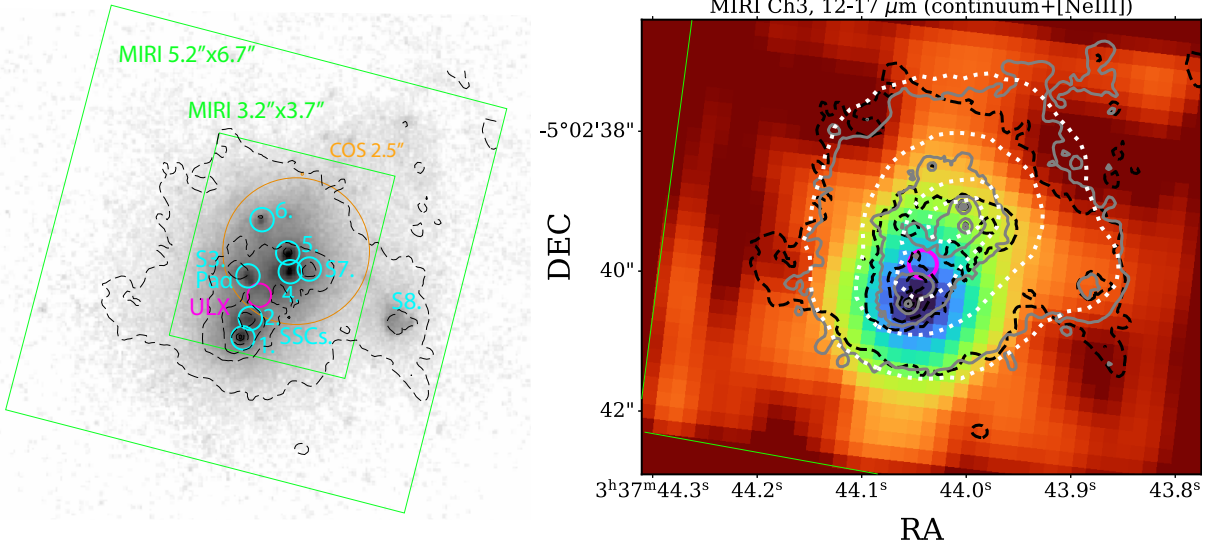


**Figure 1.** Left panel: Overview on SBS 0335-052 E ( $1'' \sim 280$  pc). HST ACS F150LP image (PID: 16209; PI Hayes) with superimposed MIRI/MRS Channel 1 and 3 FOVs, and the HST ACS WFC FR656N-F550M (PID: 10575, PI Oestlin) contours in black; the six SSCs positions (SSCs1,2,3,4,5,6,  $t \sim 3-13$  Myr; see Tab. 2) and the three further young star-forming regions (S7, S8 and S3-Pa $\alpha$ ) found by Thompson et al. (2009) are indicated; the ULX position with relative Chandra’s position uncertainty from Prestwich et al. (2013) is shown in magenta; the COS 2.5" aperture indicated in orange covers the brightest UV emitting region analyzed in the CLASSY survey (Berg et al. 2022; James et al. 2022). North is up, east is to the left. Right panel: 12-17  $\mu\text{m}$  slice from MIRI/MRS Channel 3. The log-scale color map allows highlighting of the MIRI/MRS PSF pattern due to a bright point source located close to the position of SSC1, as well as extended emission coming from the other stellar clusters. The black and grey contours show the H $\alpha$  and UV emission from the HST ACS WFC FR656N-F550M and F150LP, respectively. The white contours indicate the He II  $\lambda 4684$  emission from MUSE data (ID 096.B-0690A; PI Hayes).

(2009) by analyzing SBS 0335-052 E Pa $\alpha$  emission. The MIRI/MRS image (right panel) reveals the clear MIRI/MRS PSF pattern due to a very bright point source located at the position of SSC1 as well as extended emission covering the other stellar clusters, as we will discuss in Sec. 3.

### 3. DATA ANALYSIS AND METHODS

By a first visual inspection of the Stage 3 products, we noticed a point-source like emission dominating the continuum and emission-line fluxes close to the position of SSC1 (see Fig. 1 right panel). To spatially investigate the source of emission (Sec. 4 and Sec. 5), it was essential to determine the spatial extent of the underlying extended emission. This was achieved by accurately modeling and isolating the point source contribution, ending up with a point-source subtracted dataset and a point-source spectrum. The details of this subtraction procedure are described in App. A. In Sec. 3.1 and Sec. 3.2, we describe the data analysis applied to the point source and extended emission spectra.

#### 3.1. Emission-line fitting

In each spectrum we fitted several MIR emission lines, performing the line fitting locally around each line in a  $\pm 1000$  km/s window centered at the observed wavelength of the line of interest. In particular, we used a combination of a Gaussian profile and a one-degree polynomial to account for

emission-line and surrounding continuum emission in each spaxel of the point-source subtracted band datacube slices, as well as in the 1-D spectrum of the bright point-source and the spectrum extracted at the ULX position (shown in Fig. 1). The 1-D spectrum of the bright point source is obtained by the best-fit model of the PSF photometry analysis described in App. A, while the ULX spectrum is extracted from a region with variable diameter depending on the channel, matching the FWHM of the PSF (i.e.,  $FWHM_{Ch1,2,3,4} = 0.4'', 0.5'', 0.6'', 0.9''$  (Law et al. 2023)). Table 1 compiles the list of emission lines analyzed, together with their rest-frame wavelengths and ionization potentials (I.P.).

Fig. 2, 3 and 4 show the point source spectrum (SSC1), the spectrum extracted from the spaxels covering the ULX position, and a spectrum from the north-west region covering the clusters SSCs3,4,5,6 and S7 and the peak of UV emission (see Fig. 1), respectively, as well as the best-fit (in red) for the MIR emission lines. In the following, we consider line detections as those with fluxes with signal-to-noise (S/N) higher than 3 and upper limits for measurements with  $S/N \gtrsim 2$ . In particular, we note that emission lines typically observed in AGN (e.g., Dasyra et al. 2024), such as [Ne VI]  $\lambda 7.65$  (tentatively fitted only in the bright point source spectrum with  $S/N \lesssim 2.5$ ), [Mg V]  $\lambda 5.61$  (I.P. = 109.3 eV) and [Mg VII]  $\lambda 5.5$  (I.P. = 186.76 eV) are not detected.

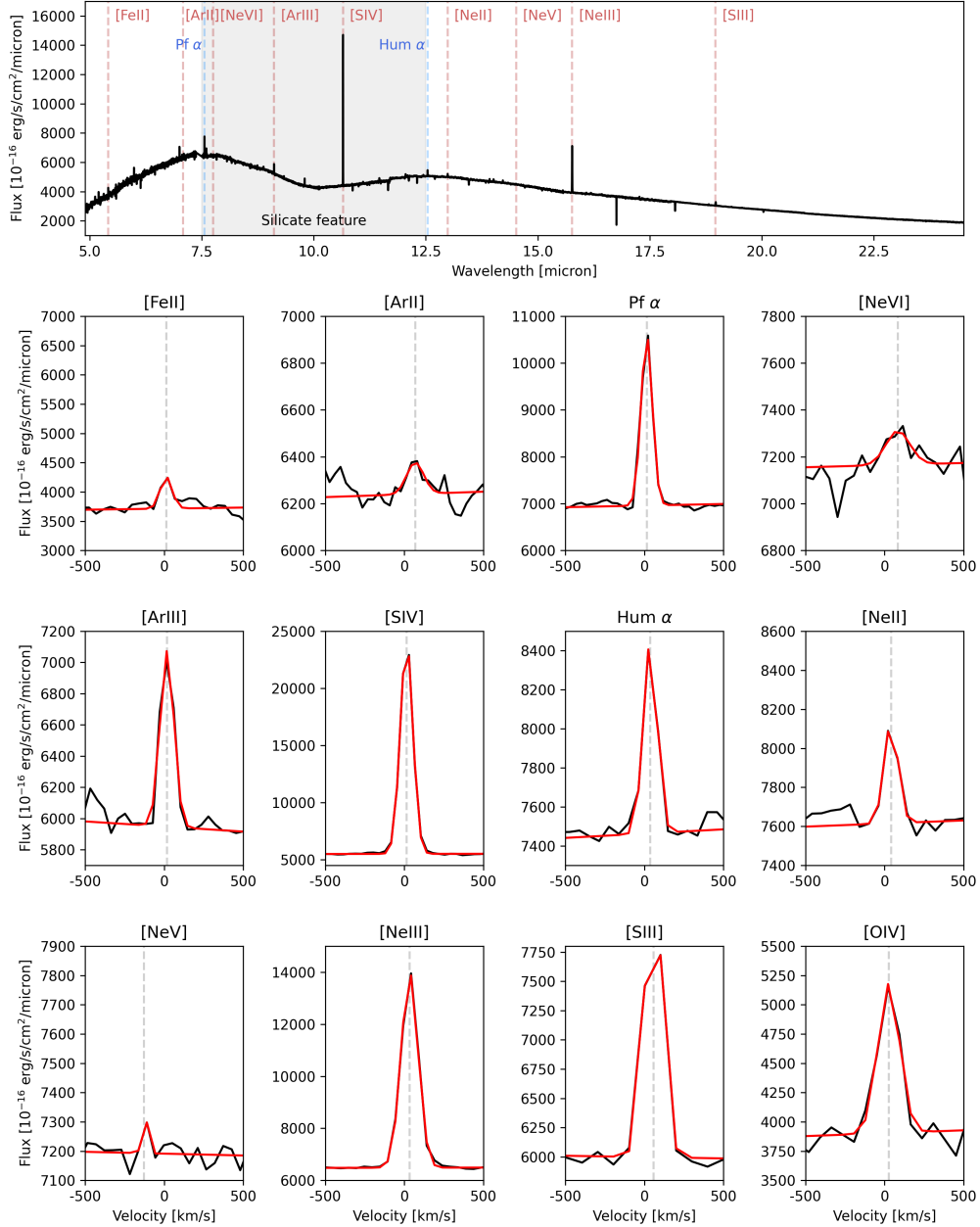


**Figure 2.** Point-source (SSC1) spectrum with the set of emission lines highlighted in blue for the hydrogen-recombination lines and red for the metallic-forbidden lines. The bottom panels display a zoom-in around each emission line considered in this work with the best-fit model shown in red. The point-source spectrum shows also a very high attenuation, with  $A_V \sim 20$ . The larger contribution of the dust can be appreciated by the silicate feature at  $9.7 \mu\text{m}$  (gray shaded area), most pronounced in the point source spectrum. [Ne VI]  $\lambda$  7.65, [Ne V]  $\lambda$  14.32 and [Ar II]  $\lambda$  6.98 have  $S/N \lesssim 2.5$ , so they cannot be considered detections. All the other lines have  $S/N > 3$ .

### 3.2. Dust attenuation

The emission-line fluxes were converted from the original MJy/sr into  $\text{erg/s/cm}^2/\text{arcsec}^2$  and corrected for the total foreground Galactic reddening along the line of sight using the  $E(B-V)$  values determined for this object by Berg et al. (2022) and the Gordon et al. (2023) dust extinction relationship.

When exploring the spectrum of the point source SSC1, we noticed a wide absorption in the  $7.5\text{-}12.5 \mu\text{m}$  range, corresponding to the silicate feature at  $9.7 \mu\text{m}$  (highlighted in grey in Fig. 2, 3 and 4). This feature (revealed also in SBS 0335-052 E Spitzer spectrum; Houck et al. 2004) pinpoints the presence of dust within this region, as already reported by Hunt et al. (2014). Thus, an intrinsic dust attenuation correction has to be applied to the line fluxes as well. Before

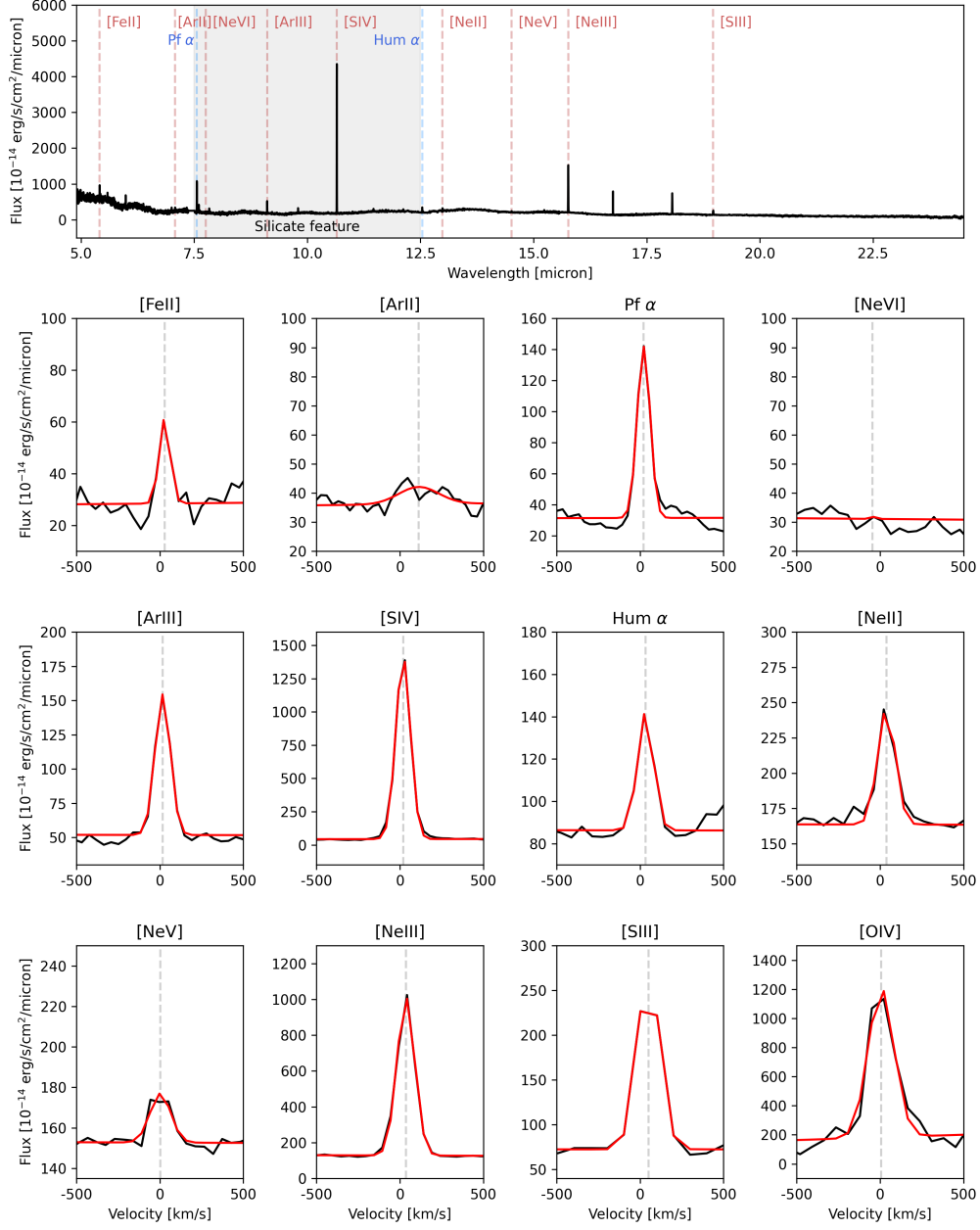


**Figure 3.** Same as Fig. 2 for the spectrum extracted at the ULX position (see Fig. 1), ULX spectrum is extracted from a region with variable diameter depending on the channel, matching the FWHM of the PSF (i.e.,  $FWHM_{Ch1,2,3,4} = 0.4'', 0.5'', 0.6'', 0.9''$  (Law et al. 2023)). [Ne VI]  $\lambda$  7.65 and [Ar II]  $\lambda$  6.98 are not detected, while all the other lines have  $S/N > 3$ .

using the continuum to determine the level of dust attenuation, there are few extra corrections we needed to implement to the datacubes. First, we limited the impact of fringing on the continuum spectra by applying an additional 1D fringing correction using the JWST pipeline tools. Also, the data exhibit discontinuities, or “jumps”, in the flux normalization among the different bands, which we corrected by fixing the normalization to Band A in Channel 1. With the continuum corrected and optimized for the analysis, we used the Contin-

uum and Feature Extraction software (CAFE, Marshall et al. 2007; Diaz-Santos et al., *in prep.*) to model the continuum of both the point-source spectrum and the point-source subtracted (extended) continuum in the range 5–20  $\mu\text{m}$  from Channel 1, 2 and 3 band datacubes (see App. A). CAFE uses a combination of blackbody emission at different temperatures together with a custom attenuation law (compatible with Gordon et al. 2023) to describe the overall shape of the continuum at near-to-mid infrared wavelengths. For the case of

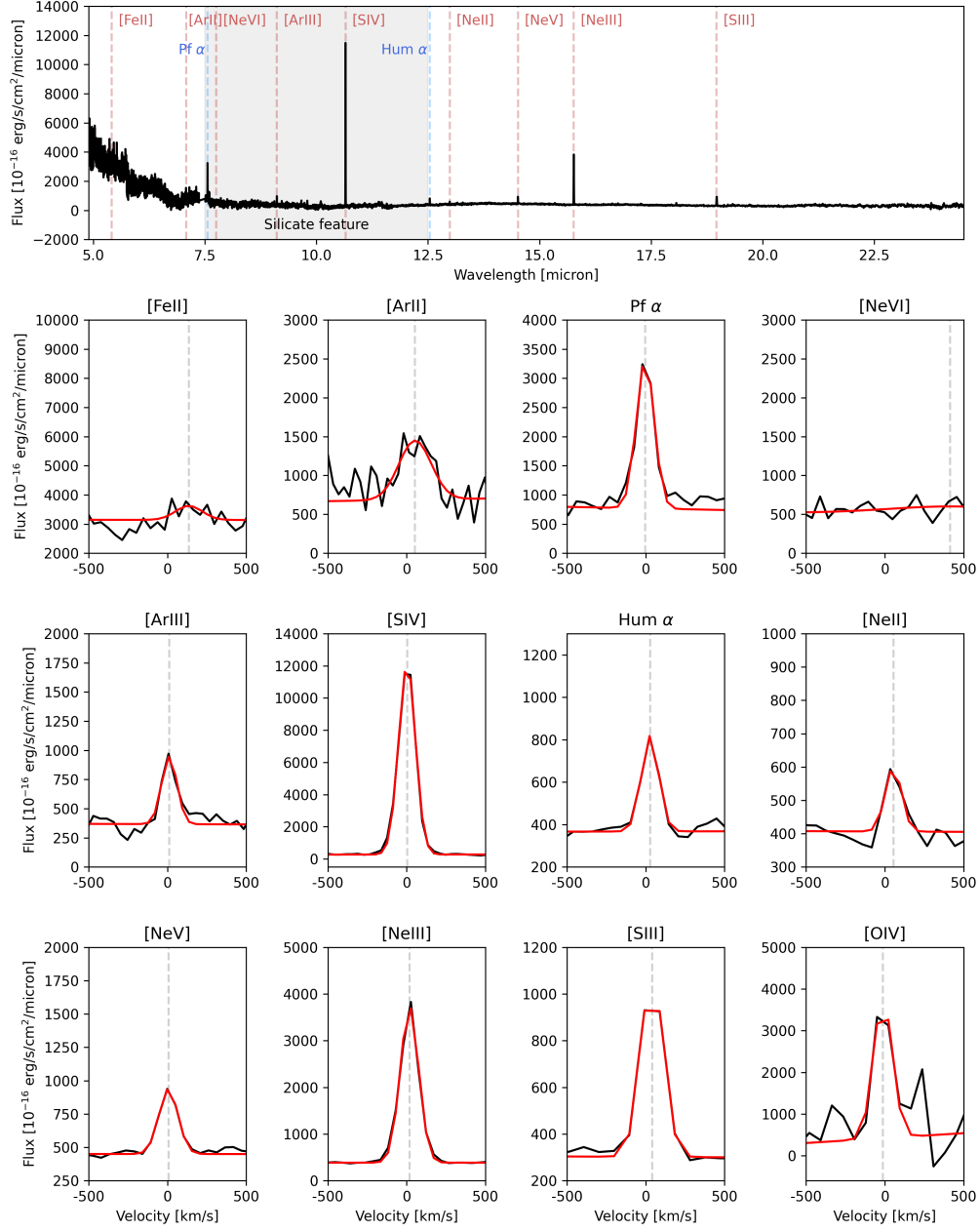


**Figure 4.** Same as Fig. 2 for the region covering the peak of the UV emission and He II  $\lambda$  emission observed with HST and MUSE, respectively (see Fig. 1). [Fe II]  $\lambda$ 5.34 and [Ne VI]  $\lambda$  7.65 are not detected, while all the other lines have  $S/N > 3$ .

SBS 0335-052 E only two dust components were considered: a cool component, whose temperature falls in the range 40-100 K, and a warm component, with temperature in the range 100-500 K. While both spectra, the point-like source and the extended emission, needed a cool component of  $T \sim 80$  K, only the point-like source required an additional warm component with  $T \sim 150$  K to model the continuum shape. A more detailed description of the dust attenuation correction will be presented in del Valle-Espinosa et al., in prep. As a result, the peak of dust attenuation corresponds to the point

source SSC1 with  $A_V \sim 20$ , while for the extended region we considered an average value of  $A_V \sim 8$ . We used the derived  $A_V$  values and the Gordon et al. (2023) dust extinction relationship to correct for intrinsic dust attenuation.

Although the extinction curve at the MIR wavelengths is almost flat, lines located in the deepest part of the silicate feature (highlighted in grey in Fig. 2, 3 and 4) can suffer from large attenuation. In the case of SBS 0335-052 E, the dust-corrected fluxes of almost every emission line are increased by a factor of  $\sim 2$  ( $\sim 1.2$ ) in the point-like source (extended)

Line	$\lambda$ ( $\mu\text{m}$ )	I.P. (eV)
[Fe II]	5.34	7.90
[Ar II]	6.98	15.76
Pf $\alpha$	7.46	13.6
[Ne VI]	7.65	126.25
[Ar III]	8.99	27.63
[S IV]	10.51	34.79
Hu $\alpha$	12.37	13.6
[Ne II]	12.81	21.56
[Ne V]	14.32	97.12
[Ne III]	15.56	40.96
[S III]	18.71	23.34
[Ne V]	24.32	97.12
[O IV]	25.89	54.95

**Table 1.** List of the fitted MIR emission lines, including their rest-wavelength and ionization potential (I.P.).

spectrum, except for the [Ar III] and [S IV] lines — which fall within the silicate feature — whose correction factor is  $\sim 3$  ( $\sim 1.6$ ). This also implies that only emission-line ratios including [Ar III] and [S IV] lines can be affected by dust attenuation.

### 3.3. PSF and pixel size matching

In this paper, we want to diagnose the main ionization source by comparing emission-line ratios and models. Since MIRI/MRS channels have a wavelength-dependent PSF and a different pixel size, we needed to convolve and rescale our emission-line maps before calculating the ratios of lines in different regions of the MIR spectrum. We avoided taking into account the complexity of the PSF profile in each sub-channel and wavelength as we did for the PSF subtraction procedure since it would have added further artefacts and uncertainties. Instead, we considered the linear relation between the MIRI/MRS PSF FWHM and  $\lambda$  found by Law et al. (2023; see their Eq. 1). Then, we convolved the line maps with a 2-D Gaussian kernel set to a value equal to the difference in quadrature of the PSF FWHMs at the wavelengths taken into account, similarly to Jones et al. (2024). Specifically, we created two sets of emission-line maps, convolving them either to the [Ne III]  $\lambda$  15.56 or the [O IV]  $\lambda$  25.89 PSFs ( $FWHM_{PSF} \sim 3$  px, 4.5 px,  $\sim 0.6''$ ,  $0.9''$ ,  $\sim 168,252$  pc, respectively). Finally, we rescaled all the emission maps to Channel 3 pixel size ( $0.245''$ ), where the majority of the emission lines taken into account in this work are located.

### 3.4. Photoionization and shock models

In order to understand the main source of ionization in Sec. 4 and Sec. 5, we compared the observed emission-line

ratios to different sets of photoionization and shock models from the literature. In particular, we considered:

- Simple stellar population (SSP) models from Martínez-Paredes et al. (2023; MP23 hereafter)<sup>1</sup>;
- SSP models with and without the ionizing output from X-ray binaries (XRBs) from Garofali et al. (2024; G24 hereafter);
- Intermediate-massive black hole (IMBH) models from Richardson et al. (2022; R22 hereafter);
- Shock models from Flury et al. (2024; F24 hereafter) and the Mexican Million Models Shock Database<sup>2</sup>, described in Alarie & Morisset (2019; AM19 hereafter).

For all these models, we considered only the two lowest metallicity grids available (i.e., 5% and 10%  $Z_{\odot}$  models for G24, R22, F24, and 2% and 10%  $Z_{\odot}$  for MP23), in accordance with SBS 0335-052 E's metallicity range (Papaderos et al. 2006; Nakajima et al. 2024). Also, we took into account only bursts of star-formation with ages below 100 Myr (upper limit on age of SBS 0335-052 E) to match SBS 0335-052 E properties (Izotov et al. 1997; Wofford et al. 2021; Berg et al. 2022; Mingozi et al. 2024, Martínez et al. in prep.). For all the grids, we consider the ionization parameter  $\log(U)$  between -4 and -1.5 (apart from R22 where  $\log(U)$  reaches -0.5). For MP23, R22 and shock models, we could also test the effect of different densities ( $n_H = 10^2 - 10^4$   $\text{cm}^{-3}$  in MP23, R22;  $n_H = 1 - 10^4$   $\text{cm}^{-3}$  in shock models), finding small differences that only slightly impact the results shown in Sec. 4, as we discuss in Sec. 5. Here below we give a summary of the characteristics of all these models.

MP23 SSP models combine CLOUDY (Ferland et al. 2017) with the revised version of the Bruzual & Charlot (2003) stellar population synthesis models introduced in Plat et al. (2019; C&B models), spanning across several parameters (see their Table 4), including a Kroupa (2001) and top-heavy (x030) initial mass functions (IMFs) with a mass range up to 100 and 300  $M_{\odot}$ . C&B models accurately cover the evolution of O and B stars, including the Wolf-Rayet (WR) phase, whose contributions last a few Myr. C&B models also include hot post-Asymptotic Giant Branch (pAGB) stars, also known as hot low-mass evolved stars (HOLMES; Stasińska et al. 2008), which emit a strong UV continuum ionizing and exciting the surrounding medium at ages between 70 and 500 Myr (peak around 100 Myr).

G24 modeled simple stellar populations (SSPs) and a population of ultraluminous X-ray sources (ULXs), combining

<sup>1</sup> Available in the Mexican Million Models Database: <https://sites.google.com/site/mexicanmillionmodels/>; <http://3mdb.astro.unam.mx:3686/>

<sup>2</sup> <http://3mdb.astro.unam.mx:3686/>



the ionizing impact of a SSP with XRBs, creating “simple X-ray populations” (SXPs). As described in detail in G24, XRBs form in multiple generations following a burst of SF ( $\gtrsim 3-5$  Myr), thus can produce ionizing photons on longer timescales than single massive stars (up to  $\sim 20$  Myr). Also, when present, they dominate the X-ray power output of star-forming galaxies and have a luminosity that scales with SFR. G24 used binary population synthesis models from Fragos et al. (2013) and burst ages ranging from 1 to 20 Myr. For the SSPs, they used the stellar population synthesis code BPASS v2.2 (Eldridge et al. 2017). Then, they created the SSP and SXP models with CLOUDY considering different values of gas-phase metallicities and ionization parameters, and a close geometry. Concerning the chemical composition of the CLOUDY models, G24 followed the prescriptions used in R22.

R22 made emission line predictions for  $10^3 - 10^4 - 10^5 - 10^6 M_{\odot}$  IMBHs with CLOUDY, taking into account two extreme spectral energy distributions (SED) - a “disk-plaw” and a “qsosed” - for the incident radiation field (see R22 Sec. 2.1) - and a starburst continuum including WR contribution, using the stellar population synthesis code BPASS v2.0 (Stanway et al. 2016) with a Kroupa IMF. To address different physical uncertainties, R22 models at different values of metallicities and ionization parameters include both coincident and non-coincident mixing of the IMBH and starlight excitation, and open and closed geometries. In particular, in this paper we show the 20 Myr instantaneous burst of star formation grids (in SSPs [O III]  $\lambda 5007/H\beta$  peaks at 20 Myr; Xiao et al. 2018), with coincident mixing and closed geometry. The line ratios do not vary significantly in the non-coincident outputs, but can be slightly affected by the choice of geometry, as we comment in Sec. 4.

AM19 shock models are made with Mappings-V (Sutherland & Dopita 2017), a plane-parallel geometry and the same prescriptions of the well-known Allen et al. (2008) models, but spanning a broad range of gas-phase metallicities and densities. F24 models are made similarly with Mappings-V, but uniformly implemented empirical abundance patterns and dust depletion treatment as well as updated atomic data. Generally, two sets of models are taken into account: pure shocks and shocks+precursor. In this work, we consider only shocks+precursor models, since they also consider the gas entering the shock front. The grids we show span values of shock velocity ( $v_s = 100 - 1000$  km/s) and the magnetic field parameter ( $B_0 = 10^{-4} - 10 \mu\text{Gauss}$ ), which are the main parameters regulating the shock ionization spectrum and the effective ionization parameter. We find that AM19 and F24 shock models behave similarly in the range of parameters considered, thus in Sec. 4 we show only F24 grids.

## 4. RESULTS

### 4.1. Emission-line maps

Fig. 5 shows the emission line maps of the extended MIR emission lines obtained after the point source subtraction:  $\text{P}\alpha$   $\lambda 7.49\mu\text{m}$ ,  $\text{H}\alpha$   $\lambda 12.37\mu\text{m}$ , [Ne II]  $\lambda 12.81\mu\text{m}$ , [S III]  $\lambda 18.71\mu\text{m}$ , [Ar III]  $\lambda 8.99\mu\text{m}$ , [S IV]  $\lambda 10.51\mu\text{m}$ , [Ne III]  $\lambda 15.56\mu\text{m}$ , [O IV]  $\lambda 25.89\mu\text{m}$ , and [Ne V]  $\lambda 14.32\mu\text{m}$ , in order of ionization potential (see Tab. 1). The maps of all the lines but [S III] and [O IV] (Channel 4;  $FWHM_{PSF} \sim 0.9''$ ,  $\sim 252$  pc) are convolved with the spatial resolution at the [Ne III] wavelength ( $FWHM_{PSF} \sim 0.6''$ ,  $\sim 168$  pc) and rescaled to Channel 3 pixel scale ( $0.245''$ ). The FOV varies from  $3.2'' \times 3.7''$ , to  $4.0'' \times 4.8''$ ,  $5.2'' \times 6.2''$  and  $6.6'' \times 7.7''$  for Channel 1 ( $\text{P}\alpha$ ), 2 ([Ar III], [S IV]), 3 ( $\text{H}\alpha$ , [Ne II], [Ne V], [Ne III]) and 4 ([S III], [O IV]), respectively. In the [S III] map panel we indicate the positions of SBS 0335-052 E several star-forming regions as we did in Fig. 1.

$\text{P}\alpha$  and  $\text{H}\alpha$  maps follow the  $\text{H}\alpha$  distribution, which peaks in young star-forming regions ( $t < 3$  Myr), such as the position of SSC1 (point source) and SSC2 as well as S7 and S3-Pa $\alpha$ , slightly shifted with respect to the other SSCs and very bright in Pa $\alpha$  (Thompson et al. 2009). [Ne III] and [S IV] have a very similar distribution with their emission extending across the MIRI/MRS FOV, due to their similar I.P. (see Tab. 1). Higher ionization emission such as [Ne V] and [O IV] mainly comes from the north-west portion of the galaxy, covering the older clusters SSCs3-4-5-6 ( $t \sim 7 - 15$  Myr) and peaks around the S7 position. The UV emission (HST ACS 150LP; Fig. 1) shows a different pattern with respect to MIR and optical hydrogen lines, tracing the six SSCs and peaking in the [Ne V] and [O IV] high ionization region. We highlight that He II  $\lambda 4686$  (similar I.P. to [O IV]) emission studied by Kehrig et al. (2018) with MUSE data closely follows the UV contours.

We notice that the peak of [Ne III] and [S IV] emission is close to the ULX position revealed by Prestwich et al. (2013; see also Kehrig et al. 2018) with Chandra (magenta circle). However, there is no clear correspondence between the ULX X-ray emission and high ionization lines, since the [Ne V], [O IV] and UV emission peaks are shifted towards S7. We highlight that the ULX extracted spectrum is also characterized by [Fe II]  $\lambda 5.34\mu\text{m}$  emission, that is not shown in Fig. 5 since it does not show clear extended emission (see Fig. 12).

The region where we subtracted the point-source emission, located at the position of SSC1, shows either a reduced or tentative emission (grey regions with  $S/N \sim 2$ ) in the line maps. This can be clearly seen in the  $\text{H}\alpha$  and [Ne V] maps. This could be due to a real lack of extended emission around SSC1 or to uncertainties in the PSF subtraction procedure. As shown in Fig. 2 the point source SSC1 shows almost all the emission lines reported in Fig. 5, apart from [Ne V] and

[Ar II]. The point source spectrum also shows clear [Fe II] emission (see also Fig. 12).

#### 4.2. Emission-line ratio maps

Fig. 6 shows [Ne III]/[Ne II], [Ne V]/[Ne II] and [O IV]/[Ne II] line ratio extended emission maps with a color-coding chosen to enhance the peak regions to aid with the interpretation of the diagnostic diagrams. [Ne III]/[Ne II] is known to be a good tracer of the ionization parameter  $\log(U)$ , while [Ne V]/[Ne II] and [O IV]/[Ne III] are found to be sensitive also to the hardness of the ionizing spectrum (Richardson et al. 2022; Garofali et al. 2024). Indeed, these line ratios do not show the same behavior. The peak of [Ne V]/[Ne II] and [O IV]/[Ne III] maps are located around region S7, aligning with the peak in  $H\alpha$  emission (see black contours). While [Ne III]/[Ne II] is also enhanced in S7, it instead peaks at the position of S3-Pa $\alpha$ , also bright in  $H\alpha$  (see black contours). SSC3, SSC4, SSC5 and SSC6 are characterized by high ionization emission, but lower [Ne V]/[Ne II] and [O IV]/[Ne III] line ratios than S7. As mentioned above, the extended region covering SSC1 (point source) and SSC2 does not have sufficient S/N in [Ne II], [Ne V] and [O IV]. Finally, S8 does not have either [Ne V] or [O IV] emission but shows intermediate values of [Ne III]/[Ne II].

#### 4.3. Ionized gas kinematics maps

Fig. 7 shows the [S IV], [Ne III] and [Ne V] velocity and intrinsic velocity dispersion maps. The velocity maps are centred on the systemic velocity of this galaxy according to previous optical studies ( $v_0 = cz \sim 4503$  km/s; Moiseev et al. 2010)<sup>3</sup>, while the intrinsic velocity dispersion maps are obtained by subtracting in quadrature the instrumental broadening dependent on wavelength from the observed velocity dispersion (see Eq. 1, Jones et al. 2023).

The MIRI/MRS FOV is limited to the central  $\sim 1$  kpc<sup>2</sup> of SBS 0335-052 E and does not cover the entire ionized gas distribution traced in  $H\alpha$  by previous studies (e.g., Moiseev et al. 2010; Herenz et al. 2023), with signs of outflowing gas extending up to  $\sim 15$  kpc (Herenz et al. 2023; in the north-west direction, along the galaxy minor axis). Thus, despite Moiseev et al. (2010) showing that on larger scales there is a disk-like north-west to south-east gradient, we only see the inner regions known to be characterized by perturbed kinematics (Izotov et al. 2006; Moiseev et al. 2010; Herenz

et al. 2017; Herenz et al. 2023). In particular, [S IV], [Ne III] and [Ne V] maps trace progressively higher ionization gas (Tab. 1) and show a consistent velocity pattern, with a blue-shifted emission around the position of S3-Pa $\alpha$  and in the north-west portion of the MIRI/MRS FOV (on the right of S7 and at the top of S8), and red-shifted emission from north to south and in the east region.

Despite the kinematic complexity shown in the velocity maps, the emission lines are well-fitted with a single Gaussian, broadening in the north-west region of the MIRI/MRS FOV. Interestingly, the [S IV], [Ne III] and [Ne V] intrinsic velocity dispersion maps seem to peak in slightly shifted positions. They all show a curious “V” shape (less visible in [Ne V]) with enhanced  $\sigma$  that peaks in SSCs 4-5 in the [Ne V] map,  $\sim 1-2$  px north than that in [Ne III] and further north in [S IV]. We notice that the region with enhanced  $\sigma$  in the [Ne V] map is located close to the peak of the [Ne V]/[Ne II] and [O IV]/[Ne II] line ratios (Fig. 6) tracing the hardening of the radiation field.

The regions where [Ne III] and [S IV]  $\sigma$  peaks probably have no [Ne V] emission due to their lower ionization (they also partly show [Ne II] emission; Fig. 5) and are characterized by enhanced red-shifted velocities, possibly showing a flow of gas moving away from the [Ne V] high ionization region. This picture is consistent with what found by Izotov et al. (2006) with high-resolution ( $R \sim 10,000$ ) VLT/GIRAFFE ARGUS spectra, showing double-peaked  $H\alpha$  profiles in the region north of SSCs 4-5 (see their Fig. 7a and 8). In particular, they interpreted these features with the presence of an expanding shell of ionized gas at  $\sim 50$  km/s, while the  $H\alpha$  broadening in SSCs 4-5 with higher dynamic activity than the surroundings.

From a visual comparison of the maps, the 15 kpc outflow revealed by Herenz et al. (2023) in  $H\alpha$  is not clearly connected to the central kpc kinematics and the location of the sources S7, SSC4-5. Interestingly, previous optical integral-field spectroscopy studies have also revealed an offset between the expanding superbubble shells and the star clusters driving the global outflow in galaxies similar to SBS 0335-052 E (e.g., Martin et al. 2024). Finally, we stress that no ionized outflow is detected in SBS 0335-052 E HST COS UV absorption lines in correspondence of the sources S7, SSC4-5 (Xu et al. 2022; Parker et al. 2024).

#### 4.4. Diagnostic diagrams

In this paper, we explore the following diagnostic diagrams widely used in the literature (see Hao et al. 2009; Weaver et al. 2010; Inami et al. 2013, but also R22, MP23, G24):

- [Ne V]/[Ne II] versus [Ne III]/[Ne II], color-coded as a function of [O IV]/[Ne III] (Fig. 8);
- [Ne III]/[Ne II] vs [S IV]/[Ne II], color-coded as a function of [O IV]/[Ne III] (Fig. 13, App. B);

<sup>3</sup> We centred the [Ne III] velocity map -24 km/s below the systemic velocity  $v_0 = cz = 4053$  km/s found by Moiseev et al. (2010). In particular, we find this specific systematic shift in  $H\alpha$  and [Ne II] (Ch. 3A), and [Ne III] (Ch. 3C) velocity maps also obtained for the Stage 3 products, so it does not depend on the point-source subtraction procedure explained in Sec. A. We suspect that this shift is not connected to the physical conditions of the gas, as it corresponds to  $\sim$  half the wavelength step in Channel 3. Also, Pf $\alpha$ , [Ar III] and [O IV], located in different channels and characterized by different I.P., show consistent velocity maps to [S IV] and [Ne V].

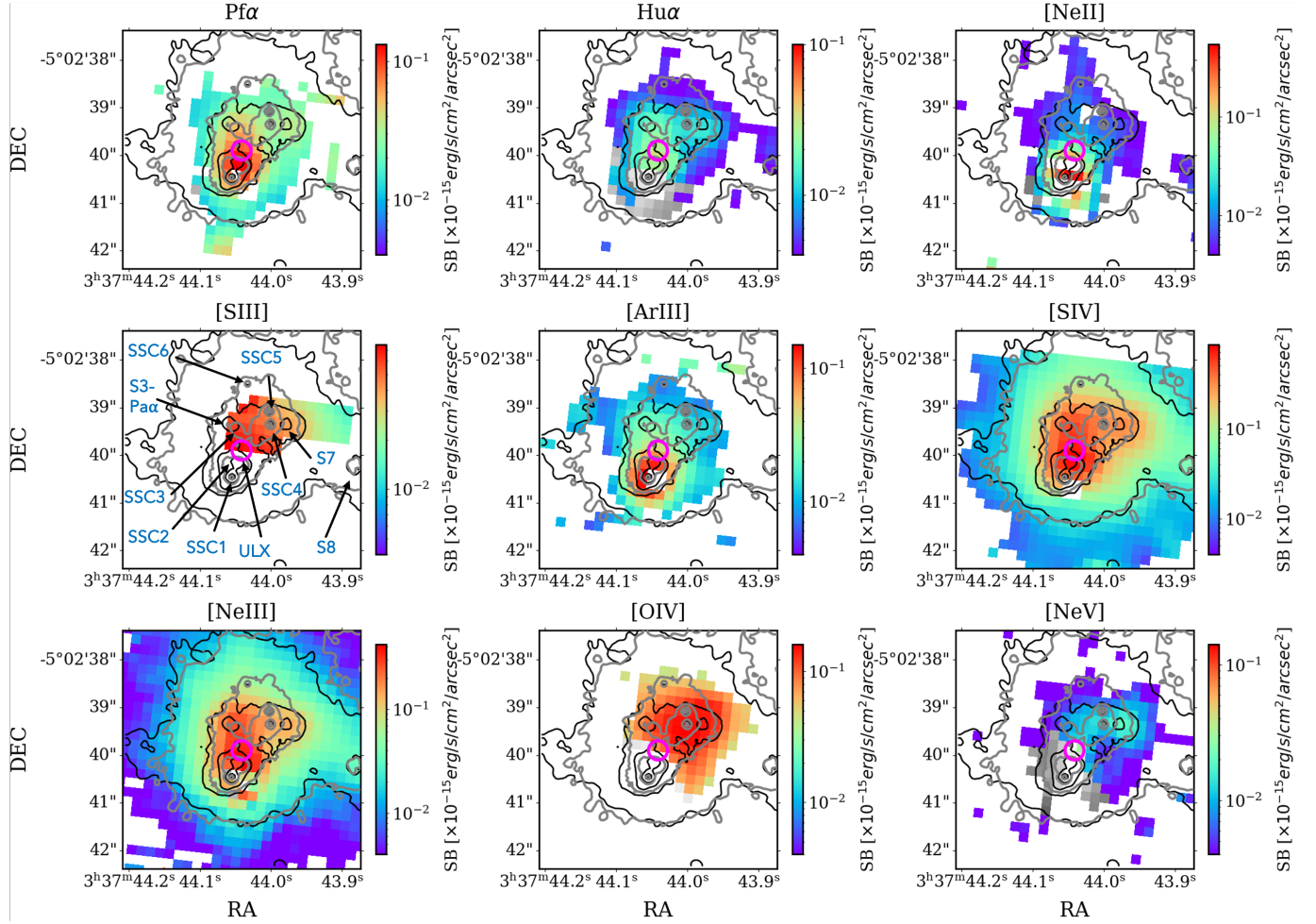


**Figure 5.** Point-source subtracted emission-line maps corrected for dust attenuation on Channel 3 pixel scale ( $0.245''$ ;  $1'' \sim 280$  pc). All lines but [S III] and [O IV] are convolved to [Ne III] resolution ( $FWHM_{PSF} \sim 0.6''$ ). The colored regions represent the measurements with  $S/N > 3$ , while the grey areas have  $S/N \sim 2$ . The black and grey contours show the  $H\alpha$  and UV emission from the HST ACS WFC FR656N and F150LP filters (PID: 10575; 16209), respectively. The magenta circle shows the position of the ULX identified in this galaxy by Chandra (Prestwich et al. 2013), taking into account a  $0.4''$  uncertainty. The emission line maps are shown in order of ionization potential (see Tab. 1). The positions of SBS 0335-052 E's several star-forming regions are shown on the [S III] map (see also Fig. 1). The extended high ionization region (bright [Ne V] and [O IV]) covers the majority of the stellar clusters and peaks around the S7 region. The FOV varies from  $3.2'' \times 3.7''$ , to  $4.0'' \times 4.8''$ ,  $5.2'' \times 6.2''$  and  $6.6'' \times 7.7''$  for Channel 1 (Pfa), 2 ([Ar III], [S IV]), 3 (Hua, [Ne II], [Ne V], [Ne III]) and 4 ([S III], [O IV]), respectively.

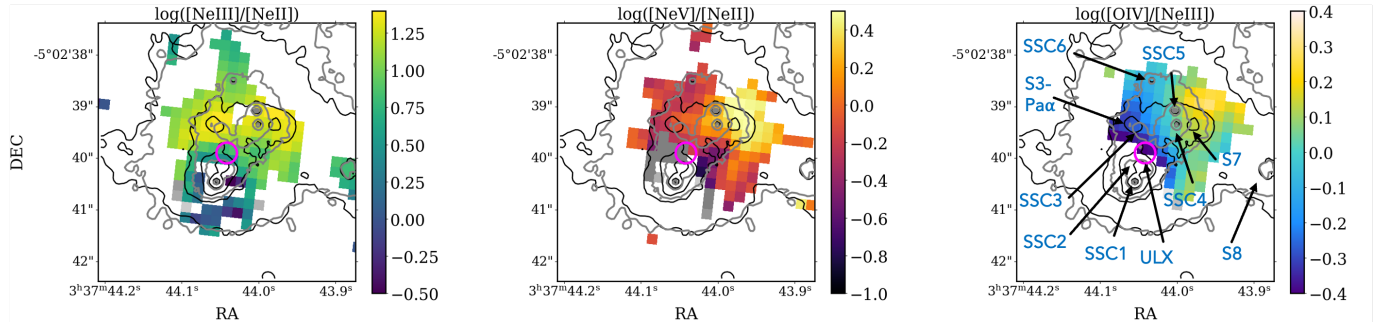


**Figure 6.** [Ne III]/[Ne II], [Ne V]/[Ne II] and [O IV]/[Ne III] line-ratio maps, where the colored spaxels have  $S/N > 3$  for the displayed emission lines. [Ne III]/[Ne II], tracing the ionization parameter, peaks around S3-Pa $\alpha$ , while [Ne V]/[Ne II] and [O IV]/[Ne III], both tracing the radiation hardness, peak close to S7. The color-coding is the same as Fig. 8, Fig. 13 and Fig. 13, to visually understand to which regions the line ratios correspond. The grey areas show regions where [Ne II] and [Ne V] have  $S/N \sim 2$ .

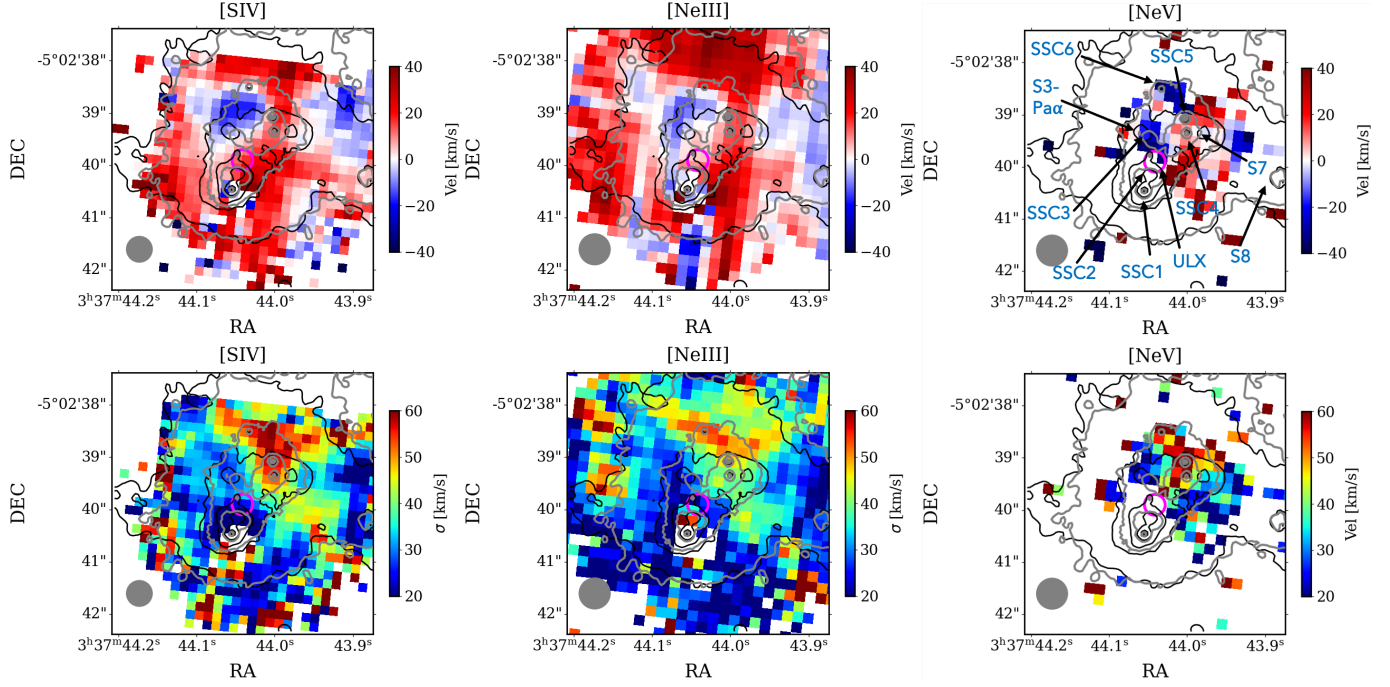


**Figure 7.** Velocity (top panels) and intrinsic velocity dispersion maps (bottom panels) of the [S IV], [Ne III] and [Ne V] emission lines, in order of ionization potential (see Tab. 1), with the same orientation, labeling and contours as Fig. 5 ( $1'' \sim 280$  pc). The velocity is centered onto the systemic velocity of the galaxy (see footnote 3). We show only the spaxels with  $S/N > 3$ . [S IV] belongs to Channel 2, [Ne III] and [Ne V] to Channel 3, and the maps are not convolved and are in their native pixel scale. The velocity maps show a similar pattern with blue-shifted emission around the S3-Pa $\alpha$  source and on the west part of the FOV, and red-shifted emission from north to south and in the east part of the FOV, possibly as a result of an expanding shell (see Izotov et al. 2006). The velocity dispersion maps show an enhancement in the north region (“V” shape) with values North from SSC4-5-S7, where we see the high ionization [O IV] and [Ne V] emission, with a slight shift to the north in the lower ionization lines. The grey circle shows the  $FWHM_{PSF}$  ( $\sim 0.5''$  for [S IV];  $\sim 0.6''$  for [Ne III] and [Ne V]) to highlight that we resolve the displayed velocity pattern and high  $\sigma$  features.

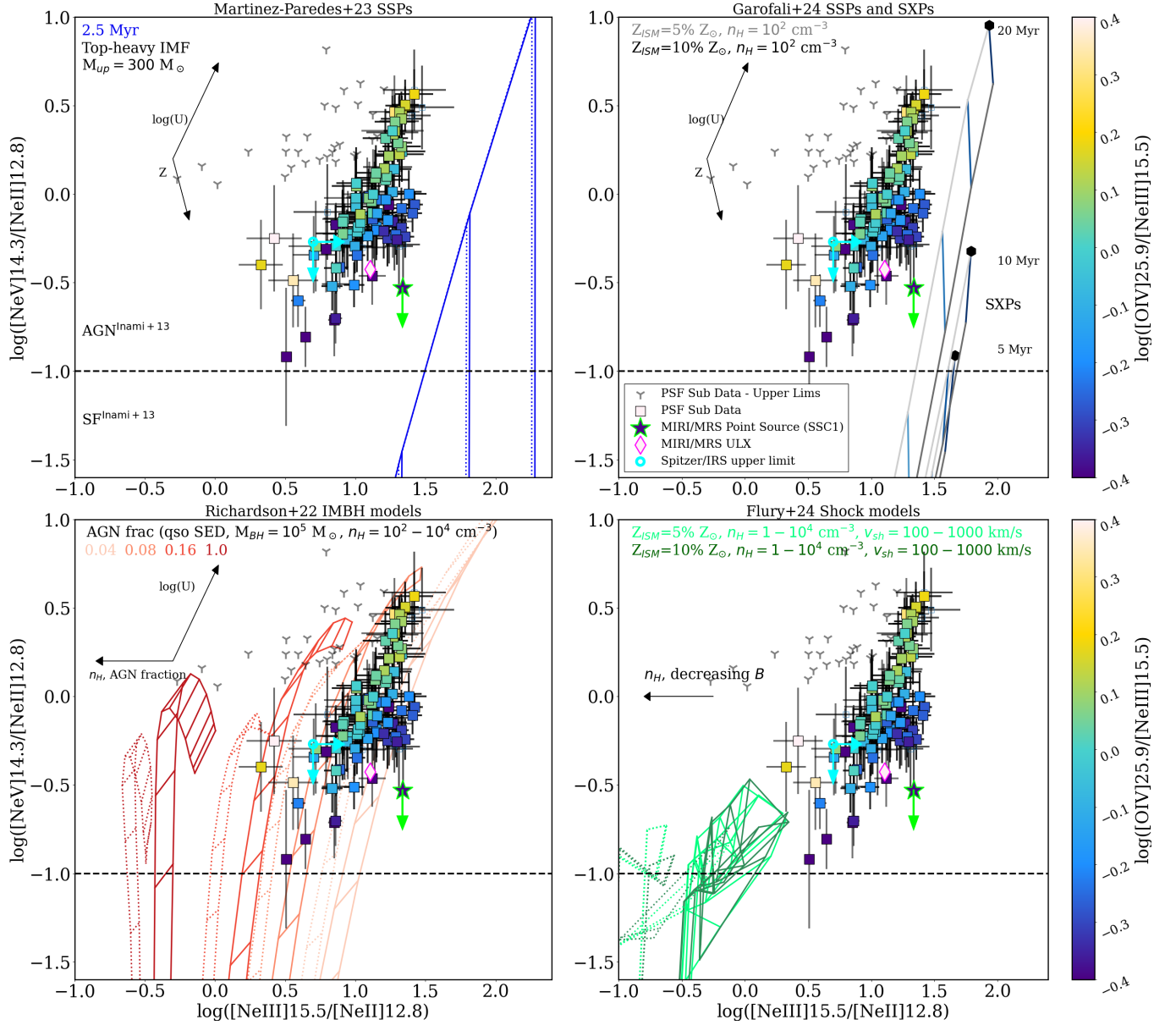


**Figure 8.** [Ne V]/[Ne II] versus [Ne III]/[Ne II] diagnostic diagram color-coded as a function of [O IV]/[Ne III] line ratio, with overplotted the four sets of low-metallicity models presented in Sec. 3.4: 2.5 SSPs models from MP23, 5, 10 and 20 Myr SSPs and SXPs models from G24, IMBH models ( $M_{BH} = 10^5 M_{\odot}$ ; 20 Myr SSP; 4%, 8%, 16%, 100% AGN fraction; close geometry) from R22 and shock+precursor models from F24. The model details are indicated in the different panels. The dotted grids have higher density. The star and diamond symbols in the scatter plots show the line ratios measured for the point source (SSC1) and the ULX spectrum, respectively. The cyan point indicates the Spitzer upper limit ([Ne V] and [Ne II] fluxes are upper limits; Houck et al. 2004; Hao et al. 2009). The black dashed line shows the criterion to separate SF from AGN from Inami et al. (2013). The grey points are upper limits ( $S/N \sim$ ; see grey regions in Fig. 6), tracing extended emission close to the point source. The models that show better agreement with the measurements are Richardson et al. (2022) IMBH models with a low AGN fraction (4–16%). This diagnostic diagram is only marginally affected by the wavelength-dependent MIRI PSF, pixel scale and dust reddening since all the lines belong to Channel 3, where the attenuation law is flat.

- [Ne III]/[Ne II] versus [O IV]/[Ne III], color-coded as a function of [Ne V]/[Ne II] (Fig. 14, App. B).

We highlight that [Ne V]/[Ne II] versus [Ne III]/[Ne II] represents the most reliable diagnostic diagram explored here, since these lines lie in Channel 3, where the attenuation law is flat, thus they are minimally impacted by PSF variations and dust correction. [S IV]/[Ne II] instead can be affected by dust reddening, while [O IV]/[Ne III] is the ratio most affected by the wavelength-dependent MIRI/MRS PSF variation correction, as well as residual fringing, given that [Ne III] is located in Channel 3c and [O IV] in Channel 4c. For these reasons, we mainly focus this section on [Ne V]/[Ne II] versus [Ne III]/[Ne II], moving the other two diagnostic diagrams in App. B.

The color-coding of each diagram corresponds to its respective map shown in Fig. 6, to visually understand to which regions the shown line ratios correspond. We decided to focus on these diagnostic diagrams for the following reasons: (i) [Ne III]/[Ne II] line ratio traces  $\log(U)$  and it can also be a good diagnostic of AGN fraction for IMBHs (R22). In general, it can widely vary in galaxies, offering a good opportunity to investigate their properties. (ii) [S IV]/[Ne II] is known to behave similarly to [Ne III]/[Ne II], given the common denominator and [S IV] and [Ne III] similar I.P. Indeed, Groves et al. (2008) found a very tight linear correlation between these line ratios that holds - with some scatter - for very different galaxies, including starbursts, ultra-luminous infrared galaxies, AGN, and also BCDs such as SBS 0335-052 E. As such, we can use these line ratios to test how SBS 0335-052 E compares to similar BCDs. (iii) [O IV] and [Ne V] instead are high ionization emission lines (see Tab. 1), usually considered good indicators of ionizing mechanisms beyond SF, such as AGN and IMBHs. In particular, as mentioned in Sec 4.2, both [O IV]/[Ne III] and [Ne V]/[Ne II] are able to trace the hardness of the ionizing spectrum (R22; G24). For instance, a typical criterion to differentiate AGN from SF dominated galaxies is  $\log([\text{Ne V}]/[\text{Ne II}]) > -1$ , given the much lower ionization potential of [Ne II], abundantly produced in H II regions (e.g., Inami et al. 2013). Also, [Ne V] is usually undetected in pure-star-forming regions, and difficult to reproduce even with SXP models (e.g., only at specific  $\log(U)$  and  $Z$ ; see G24). A criterion to distinguish SF and IMBHs ionization was proposed by Richardson et al. (2022), introducing separators according to [O IV]/[Ne III] and [Ne III]/[Ne II] line ratios.

Fig. 8 (same for Fig. 13 and Fig. 14, App. B) show four panels where we overlay the diagnostic diagrams with a different set of low-metallicity models (see Sec. 3.4):

- MP23 2.5 Myr SSPs, with top-heavy IMFs and  $M_{up} = 300 M_{\odot}$  (upper left panel);

- G24 SSPs and SXPs grids at 5, 10 and 20 Myr (upper right; the hexagon represents the highest line ratio each grid can reproduce);
- R22 IMBHs grids with  $M_{BH} = 10^5 M_{\odot}$ , qso SED and 20 Myr SSP, with closed geometry and 4, 8, 16 and 100% AGN fraction, highlighting that beyond 16% the SED is completely dominated by the IMBH (lower left panel);
- F24 shock models with precursor (lower right panel).

It should be noted that for the MP23 SSP grids, the low metallicity 2.5 and 100 Myr SSPs show the highest line ratios for young and old stars, respectively. These two grids are the only ones (partially) able to cover the x- and y- ranges shown. However, we discarded the 100 Myr grid because old stars struggle to explain the observed number of ionizing photons observed in this system as we discuss in Sec. 5.2.1. Also, we notice that the choice of the IMF does not affect the line ratios, but the choice of  $M_{up} = 300 M_{\odot}$  strongly enhances [Ne V]/[Ne II]. All the other MP23 grids and G24 SSPs and SXPs grids below 5 Myr fall outside the shown x- and y- ranges. R22 IMBHs grids with  $M_{BH} = 10^{3-4} M_{\odot}$  are also not shown because they cannot reproduce  $\log([\text{Ne III}]/[\text{Ne II}])$  higher than  $\sim 0 - 0.5$ . The grids with  $M_{BH} = 10^6 M_{\odot}$  instead can overlap to the observed line ratios at 8% AGN fraction, but at lower/higher fractions, they predict larger/lower [Ne III]/[Ne II].

Fig. 8 (same for 13 and 14) scatter plots show the extended emission measured with our data (down-pointing arrows for upper limits), as indicated in the legend. We stress again that the point source (star symbol) has only tentative [Ne V] with  $S/N \sim 2$ . The cyan point indicates the [Ne V] and [Ne II] upper limits and the [Ne III] and [O IV] detections from Spitzer flux measurements (Houck et al. 2004; Hao et al. 2009), which cover the entire region covered by MIRI/MRS. In particular, Houck et al. (2004) reported that the Spitzer image had a prominent diffraction ring and was thus indistinguishable from the image of a point source (possibly SSC1 as we reveal in our data).

From a quick look at Fig. 8 (same for Fig. 13, App. B), all SBS 0335-052 E MIR line ratios lie outside of the ‘‘canonical’’ SF locus, ending in the ‘‘AGN’’ designated region according to Inami et al. (2013) and Richardson et al. (2022) criteria (see also e.g., Goold et al. 2024). This is already suggested by Spitzer upper limits (cyan point), but with MIRI/MRS data we can tell much more about the conditions of the ionized gas on a spatially resolved basis. Clearly, the [Ne III]/[Ne II] and [Ne V]/[Ne II] diagnostic diagram disentangles increasing ionization parameter and radiation hardness sequences, with both [Ne III]/[Ne II] and [Ne V]/[Ne II] progressively increasing with the  $\log(U)$  of different models (i.e., following the  $\log(U)$  arrow shown in the various panels). [Ne V]/[Ne II]

and [O IV]/[Ne III] (color-coding), being more sensitive to the radiation hardness, increase also along the perpendicular direction of the increasing  $\log(U)$  arrow, at decreasing [Ne III]/[Ne II] values. This effect is reproduced by harder ionization in the models, such as lower gas metallicity or older star ionization in SSPs models, and higher AGN fractions in IMBH models.

Another important takeaway from the top two panels of Fig. 8 (same for Fig. 13 and 14, App. B) is that all the low-metallicity young SSPs grids struggle to reproduce the observed MIR emission line ratios of SBS 0335-052 E. This suggests the need for a further ionization source. However, SXP models, including the contribution of X-ray binaries, show similar limitations. The only models that can reproduce SBS 0335-052 E MIR [Ne V]/[Ne II], [Ne III]/[Ne II] and [S IV]/[Ne II] line ratios are models including the contribution of an IMBH (4–16%), spanning a range of  $\log(U)$ . However, we highlight that these IMBH models still struggle to reproduce the highest [O IV]/[Ne III] line ratios (Fig. 14). Literature BCDs [S IV]/[Ne II] vs [Ne III]/[Ne II] observed with Spitzer follow the Groves et al. 2008 empirical relation shown in Fig. 13 (magenta line). This indicates that low-metallicity SSP, SXP and shock grids generally struggle to reproduce BCDs' lower ionization MIR lines than [Ne V].

Given the critical densities of the MIR lines, another property that can affect the parameter space covered by these line ratios is the gas density. For instance, [Ne V]  $\lambda 14.3$  is part of a doublet, showing a second transition at  $24.3 \mu\text{m}$ , with lower critical density ( $n_{\text{crit}} = 3 \times 10^4, 5 \times 10^5 \text{ cm}^{-3}$  at  $24.3, 14.3 \mu\text{m}$ ). This makes increasing [Ne V]  $\lambda 14.3$ /[Ne V]  $\lambda 24.3$  ratios a good electron density ( $n_e$ ) diagnostic in the range  $n_e = 10^2 - 5 \times 10^5 \text{ cm}^{-3}$  (e.g., Fernández-Ontiveros et al. 2016). We do not detect [Ne V]  $\lambda 24.3$ , which could be either due to the worsening of fringing in Channel 4 or to a high density of the [Ne V] emitting region. We favor the latter explanation given the fact that the [Ne V] emitting region shows high density according to previous UV and optical studies (i.e.,  $n_e(\text{[Fe III]}) = 2440 \pm 506$ ;  $n_e(\text{C III}) = 4258 \pm 1067$ ;  $n_e(\text{[Ar IV]}) = 1107 \pm 5$ ;  $n_e(\text{N IV}) < 42000$ ; Mingozzi et al. 2022). Interestingly, only models with  $n_e \sim 10^{3.5} - 10^4 \text{ cm}^{-3}$  seem able to reproduce a [Ne V]  $\lambda 14.3$  stronger than [Ne V]  $\lambda 24.3$ . However, these high-density grids are slightly shifted towards lower [Ne III]/[Ne II] and [O IV]/[Ne III] line ratios (dotted grids in all diagrams), and therefore tend to make the models less consistent with the data.

Overall, all these considerations suggest that none of the current state-of-the-art models can perfectly match our observed MIR line ratios. In Sec. 5, we discuss the feasibility of these results, also comparing them with previous spatially resolved studies performed on this galaxy.

## 5. DISCUSSION

As shown in the previous sections (see also Fig. 1, right panel), the MIRI/MRS data of SBS 0335-052 E are characterized by a bright point source emission, clearly showing the instrument PSF structure. As explained in Sec. 3 and App. A, we were able to model the point source contribution and accurately separate it from the underlying extended emission. Tab. 2 shows a summary of the information that MIRI/MRS can give us on the several star-forming regions of SBS 0335-052 E, as well as information gathered from the many previous works in the literature on this intriguing object to help with the interpretation of our data and the models presented in Section 3.4. In the following subsections, we discuss the origin of the point source and extended emission, their main ionization sources and we connect our results with the high- $z$  universe.

### 5.1. The bright point source, SSC1

As introduced in Sec. 3, the point source is the source SSC1 (Fig. 1). SSC1 appears as a point source in the MIRI/MRS data possibly because of its dusty nature, which makes it particularly bright in the MIR. As described in Sec. 3.2, when analyzing the MIR continuum, we find a very high attenuation for the point source spectrum ( $A_V \sim 20$ ). Indeed, as shown in Fig. 2, this spectrum is characterized by the silicate feature at  $9.7 \mu\text{m}$ , which is much fainter in the other regions of the galaxy. This is consistent with the fact that Hunt et al. (2014) revealed dust continuum emission uniquely coming from the region around SSC1 using ALMA data (see their Fig. 1). This region is also uniquely characterized by  $H_2$  emission, tracing warm molecular gas, as first revealed by NICMOS data (Reines et al. 2008; Thompson et al. 2009). We confirm this with our data, observing several  $H_2$  rotational transitions around SSC1 (from S(1) to S(7)), which will be modeled and discussed in detail in a forthcoming paper (del Valle-Espinosa et al., in prep.). However, the  $H_2$  emission may come from a more extended region, given that the  $H_2$  spatial distributions do not show the PSF pattern (see also Thompson et al. 2009; their Fig. 3). The point source region and close surroundings also show high  $H\alpha$  and  $\text{Pa}\alpha$  equivalent widths (Reines et al. 2008) and purely thermal radio free-free emission, which has been interpreted as due to active star-formation in a dense environment (i.e.,  $\sim 12,000 \text{ O7.5 V stars}$ ,  $n_e \sim 10^3 - 10^4 \text{ cm}^{-3}$ ,  $SFR \sim 1.3 \text{ M}_\odot/\text{yr}^{-1}$ ; Johnson et al. 2009).

It should be noted that SSC1 also displayed typical PSF Airy ring in HST Near Infrared Camera and Multi-Object Spectrometer (NICMOS) NIR data, tracing  $\text{Pa}\alpha$  and  $1.6 \mu\text{m}$  continuum emission ( $0.2''/\text{px}$ , comparable to MIRI/MRS) in Reines et al. (2008); Thompson et al. (2009). In particular, Thompson et al. (2009) showed that high-resolution ( $0.075''/\text{px}$ ) NICMOS camera 2 data could resolve the SSC1

Region	Age [Myr]	Mass [ $M_{\odot}$ ]	12+log(O/H)	Notable features	
SSC1	3.0	$4.7 \times 10^5$	7.31	Point source in MIRI-MRS and NICMOS 1.6 $\mu\text{m}$ (T09)	
SSC2	3.0	$3.7 \times 10^5$		SSC1-2 uniquely has dust and H <sub>2</sub> , and thermal radio emission (J09)	
SSC3(+S3-Pa $\alpha$ )	7.0	$7.1 \times 10^5$	7.31	WR Blue bump (P06; K18)	
SSC4	11.0	$1.1 \times 10^6$	7.27	SSCs4-5 characterized by $\sigma$ ([Ne V]) peak and tentative radio emission (J09)	
SSC5	13.0	$2.9 \times 10^6$		Point source in NICMOS 1.6 $\mu\text{m}$ (T09)	
SSC6	11.0	$2.6 \times 10^5$	—	Point source in NICMOS 1.6 $\mu\text{m}$ (T09); $\sigma$ ([S IV]) and $\sigma$ ([Ne III]) peak	
S3-Pa $\alpha$	< 3(?)	—	7.38	Bright H lines (T09)	
S7	< 3(?)	—	7.10	Bright H lines (T09); [Ne V]/[Ne II] and [O IV]/[Ne III] peak	
S8	—	—	7.21	×	
ULX	—	—	—	Revealed by P13 (see also K18)	

Region	[Ne III]/[Ne II]	[Ne V]/[Ne II]	[O IV]/[Ne III]	[S IV]/[Ne II]	[Ne V] $\lambda$ 14.3 $\mu\text{m}$
SSC1	$1.34 \pm 0.03$	< -0.53	$-0.40 \pm 0.07$	$1.71 \pm 0.03$	×
SSC2	$-0.13 \pm 0.01$	< -1.49	$-0.7 \pm 0.5$	$0.546 \pm 0.004$	×
SSC3+S3-Pa $\alpha$	$1.36 \pm 0.01$	$-0.14 \pm 0.02$	$-0.29 \pm 0.01$	$1.64 \pm 0.01$	✓
SSC4-5	$1.19 \pm 0.04$	$0.16 \pm 0.04$	$0.05 \pm 0.01$	$1.64 \pm 0.03$	✓
SSC6	$0.85 \pm 0.04$	$-0.20 \pm 0.04$	$-0.07 \pm 0.02$	$1.18 \pm 0.03$	✓
S7	$1.31 \pm 0.02$	$0.35 \pm 0.02$	$0.11 \pm 0.01$	$1.66 \pm 0.02$	✓
S8	$0.60 \pm 0.08$	—	—	$1.08 \pm 0.04$	×
ULX	$1.11 \pm 0.02$	$-0.43 \pm 0.04$	$0.48 \pm 0.02$	$1.14 \pm 0.02$	✓

**Table 2.** Ages and masses from Reines et al. (2008); Adamo et al. (2010); 12+log(O/H) from Thuan et al. (2004); Papaderos et al. (2006) with uncertainties of  $\sim 0.02$  dex; other properties from Papaderos et al. (2006); Thompson et al. (2009); Johnson et al. (2009); Prestwich et al. (2013); Kehrig et al. (2018; P06,T09,J09,P13,K18) and this work. All MIR line ratios are in logarithmic format.

emission and estimated the point source emitting region to be  $\sim 18$  pc. Thompson et al. (2009) showed that also SSC5 and SSC6 show a point source structure in the NIR NICMOS 1.6  $\mu\text{m}$  continuum, with SSC5 seeming so compact (spatial extension of  $\lesssim 10$  pc) that could not be resolved even in their high-resolution NICMOS dataset. In our MIRI/MRS data, we do not reveal any point source emission corresponding to SSC5 and SSC6, implying that those regions of the galaxy are instead dominated by extended emission in the MIR.

All the elements listed above seem consistent with SSC1 being a very young embedded star-forming region (Hunt et al. 2001; Reines et al. 2008; Adamo et al. 2010). Indeed, as shown in Fig. 8 and 14, a subset of 2.5 Myr SSP models from MP23 could tentatively explain the point source [Ne III]/[Ne II] and [O IV]/[Ne III] line ratios - despite the fact that they fall in the “AGN” regions of the diagnostic diagrams - and possibly the [Ne V]/[Ne II] upper limit. However, SSP models, are not capable of reproducing the corresponding lower ionization [S IV]/[Ne II] line ratio (see Fig. 13), which seems more consistent with R22  $M_{BH} = 10^5 M_{\odot}$  grids with an AGN fraction below 8%.

Interestingly, the point source spectrum is also characterized by [Fe II] emission, mainly located around SSCs1-2. [Fe II] is considered an important shock tracer, because of (i) its many levels with low excitation energies easily excited in shocked gas, (ii) its low ionization potential (Tab. 1) that can make it ionized by FUV radiation from the shock front

in the neutral H gas and (iii) is enhancement could be due to grain destruction by shocks (e.g., Koo et al. 2016 and references therein). However, 5-10%  $Z_{\odot}$  shock models cannot reproduce the observed MIR line ratios.

Finally, as we will discuss in detail in Sec. 5.2, Kehrig et al. (2018) derived SBS 0335-052 E He II  $\lambda$ 4686-ionizing budget (including at the position SSCs1-2; knot B in their nomenclature), finding that it can only be produced by either single, rotating metal-free stars or a 0.05%  $Z_{\odot}$  binary population and a top-heavy IMF. Since He II and [O IV] have similar I.P., they are likely powered by the same ionizing source, which could also cause the lower ionization MIR emission. However, a 0.05%  $Z_{\odot}$  (or lower) metallicity is extremely low and does not match with the gas-metallicity measured in this object (i.e.,  $\sim 5\%$   $Z_{\odot}$ ; Thuan et al. 2004; Papaderos et al. 2006; Izotov et al. 2006), making this scenario unlikely.

Overall, there is not a straightforward explanation to justify all the characteristics of the point source SSC1 emission. Having said that, the models that can simultaneously explain the MIRI/MRS [O IV]/[Ne III], [Ne III]/[Ne II] and [S IV]/[Ne II] are R22 IMBH models (see Fig.13 and 14). While these grids are unable to predict the low [Ne V]/[Ne II] upper limit, we cannot completely exclude that [Ne V] upper limit is underestimated since the point source spectrum is affected by residual fringing in Channel 3.



### 5.2. Origin of the highly ionized extended emission

As shown in Fig. 5, SBS 0335-052 E is characterized by extended high ionization emission lines such as [O IV]  $\lambda$ 25.89 and [Ne V]  $\lambda$ 14.3, localized mainly in the north-west region of the galaxy, covering SSCs 3-4-5-6 and S7 (all older than the point source SSC1; see Tab. 2), with a peak of high ionization emission located in the proximity of S7. We highlight that [Ne V]  $\lambda$ 14.3 has never been detected in BCDs before and SBS 0335-052 E's  $\log([\text{Ne V}]/[\text{Ne II}]) > 0$  values are higher than any upper limits proposed for BCDs (e.g., Hao et al. 2009), probably because of the insufficient sensitivity of ISO and Spitzer. However, its optical counterpart (i.e., [Ne V]  $\lambda$ 3426) has been previously detected in a subgroup of BCDs, including SBS 0335-052 E (see Izotov et al. 2004; Thuan & Izotov 2005; Izotov et al. 2012; 2021; Berg et al. 2021), which is the lowest metallicity object in which this line has been detected so far. [Ne V]  $\lambda$ 3426 (as well as [Ne V]  $\lambda$ 14.3,24.3) is usually considered a convincing proof of AGN activity (e.g., Abel & Satyapal 2008; Mignoli et al. 2013), powered by the hard non-thermal AGN radiation, but has also been generally justified with radiative shock models in BCDs, using Allen et al. (2008) models at solar and SMC (i.e., 20%  $Z_{\odot}$ ) metallicities (e.g., Izotov et al. 2012; 2021). However, as shown in Fig. 8, 13 and 14,  $\log([\text{Ne V}]/[\text{Ne II}]) > 0$  and enhanced  $\log([\text{O IV}]/[\text{Ne III}])$  cannot be explained by current state-of-the-art shock models at SBS 0335-052 E's metallicity (i.e.,  $\sim 5\% Z_{\odot}$ ).

The difficulty in accounting for SBS 0335-052 E's extended high ionization emission was first described by Herenz et al. (2017), who showed a nebular He II  $\lambda$ 4686 map from MUSE that brightened towards the north-west at the rim of a starburst driven super-shell (see also Kehrig et al. 2018), the He II shell that is out of our MIRI/MRS FOV. In the following sections, we discuss in detail the different scenarios which can explain the sources of the extended MIR emission, drawing insights from previous studies. In particular, it is important to consider that [O IV] has a similar I.P. to He II ( $> 4$  ryd), while [Ne V] requires the presence of even harder radiation ( $> 7.1$  ryd), corresponding to the extreme ultraviolet and soft X-ray range.

#### 5.2.1. Pure Bursts of Star Formation

MP23 and G24 SSP models considered in this work, fail to reproduce SBS 0335-052 E [Ne V]/[Ne II], [Ne III]/[Ne II], [S IV]/[Ne II] and [O IV]/[Ne III] line ratios, despite using different stellar libraries and IMFs (see Sec. 3.4). This is not unexpected considering previous studies of this system.

As mentioned previously in Sec. 5.1, Kehrig et al. (2018) was only able to derive SBS 0335-052 E's He II-ionizing budget via either single, rotating metal-free massive stars ( $\sim 200 M = 150 M_{\odot}$  stars, see their Sec. 5.3.1) or a binary population with 0.05%  $Z_{\odot}$  metallicity and a top-heavy

IMF (modeled with BPASS; see their Sec. 5.3.2). However, a 0-0.05%  $Z_{\odot}$  metallicity is unphysically low for SBS 0335-052 E (see also Wofford et al. 2021), making this scenario unlikely. Kehrig et al. (2018) discarded also Wolf-Rayet (WR) stars - massive stars ( $> 25 - 30 M_{\odot}$ ) with strong winds (e.g., Schaerer & Vacca 1998) - as the main source of ionization. Despite WR features being observed in this galaxy (in S3 and in the south-west region of the galaxy, below S8; Papaderos et al. 2006; Izotov et al. 2006; Kehrig et al. 2018), the large number needed to justify the He II-ionization budget ( $> 7000$ ) would overcome by a factor of 5-7 the SSCs total mass, depending on the IMF choice (Kehrig et al. 2018). The same argument allows us to discard WRs as the main source of [O IV] and thus [Ne V] emission.

Wofford et al. (2021; see their Sec 3.1) proposed the presence of very massive stars (VMSs) - stars with masses above  $100 M_{\odot}$  (Vink 2012) - from the blue-shifted [O V]  $\lambda$ 1371 detection in HST COS data, covering a 2.5" circular region centered on the peak of the UV emission (see Fig. 1). Thus, one might suspect that VMSs might represent the definite answer, hardening the radiation field and enabling highly ionized extended emission. However, VMSs, while hot and luminous, are known to have dense winds which become optically thick at the short wavelengths needed to power He II and [Ne V] ionizing photons, as demonstrated by Sander (2022; see also Hawcroft et al. 2025, submitted). Although, a mechanism for the enhanced escape of the hard ionizing radiation from these winds has recently been proposed by Roy et al. (2025), whereby the winds of massive stars are inhomogeneous due to intrinsic instabilities of the outflow. Roy et al. (2025) propose that the higher the degree of inhomogeneity in the outflow, the higher the emergence of extreme UV fluxes. While this possibility has not yet been comprehensively evaluated, it may motivate revisions of stellar population models in the future.

Finally, a completely different scenario to explain the high ionization extended emission could be older ionizing stars, as suggested by previous works (e.g., Izotov et al. 1997; 2006). MP23 low-metallicity SSPs models with ages of  $t \geq 100$  Myr (upper limit on age of SBS 0335-052 E; Izotov et al. 1997; Papaderos et al. 1998), would be dominated by post-AGB stars (specifically HOLMES) that could be capable of ionizing the gas with their strong UV continuum (Stasińska et al. 2008). Indeed, MP23 (see their Fig. 2) showed that HOLMES have the peak production rate of H-ionizing photons exactly at 100 Myr. Interestingly, MP23 low-metallicity 100 Myr SSP models would perfectly lie on the observed [Ne V]/[Ne II], [Ne III]/[Ne II], [S IV]/[Ne II] and [O IV]/[Ne III] line ratios shown in Fig. 8, 13, 14. However, these models were disregarded because the maximum production of ionizing photons is  $\sim 10^{43}$  photons  $s^{-1}$  for a  $1 M_{\odot}$  stellar population at SBS 0335-052 E metallicity - im-

plying that too large a population of HOLMES would be needed to match the ionization budget estimated by [Kehrig et al. \(2018\)](#); i.e.,  $Q(H) \sim 3.86 \times 10^{53}$  photons  $s^{-1}$ ). While these stars cannot be easily observed in a galaxy as distant as SBS 0335-052 E, they are not revealed in large numbers even in nearby elliptical galaxies with a weak UV excess (e.g., [Brown et al. 2008](#)), suggesting that they do not represent a significant source of UV emission as proposed.

Overall, we have discussed how state-of-the-art SSPs are not capable of reproducing high ionization extended emission observed in SBS 0335-052 E. We also highlight that SSPs struggle to explain lower ionization MIR line ratios, such as [S IV]/[Ne II] versus [Ne III]/[Ne II] (see Fig. 13), even for values typically observed in BCDs with Spitzer (i.e., [Groves et al. 2008](#) relation in magenta). This implies either a general hindering problem in low metallicity massive stars in current stellar libraries or the real need for a further source of ionization in galaxies like SBS 0335-052 E.

### 5.2.2. Ultra Luminous X-ray sources

A ULX is observed in SBS 0335-052 E ([Prestwich et al. 2013](#)), as shown in Fig. 1. In particular, ULX sources are X-ray binaries with  $L > 10^{39}$  erg/s and the ULX fraction seems to anti-correlate with gas-phase metallicity (e.g., [Mapelli et al. 2010; 2011; Prestwich et al. 2013](#)). This could suggest that, given the characteristic low-metallicity gas of BCDs, ULXs could indeed play a role in their high-ionization emission.

The contribution of these X-ray sources were accurately included for the first time in the SXP grids of [G24](#), which overlap with the range of [Ne V]/[Ne II] ratios (including the values of the spectrum extracted at the ULX position, magenta diamond) observed in SBS 0335-052 E at the highest ionization parameter values (i.e.,  $\log(U) \sim -1.5, -1$ ) and for stellar population ages between 5 Myr and 20 Myr (see Fig. 8). However, the same grids over-predict the corresponding [Ne III]/[Ne II] line ratios and, moreover, are not capable of reproducing  $\log([O\ IV]/[Ne\ III]) > 0$  that we observe (Fig. 14). We stress that [G24](#) state-of-the-art model prescriptions could suffer from some inherent assumptions, such as the assumed theoretical scaling relationships linking X-ray luminosity with age and metallicity, while observationally there is significant scatter (see e.g., [G24](#) Fig. 1).

Another factor to consider is that the ULX location determined by [Prestwich et al. \(2013\)](#) does not correspond to either the peak of the high ionization emission that we observe in the MIR or to the peak of the He II and UV emission. Indeed, [Kehrig et al. \(2018\)](#) (see also [Wofford et al. \(2021\)](#)) discarded the ULX as a possible source of He II ionization. In particular, analyzing Chandra data (see also [Thuan et al. 2004](#)) they estimated the effective ionizing power at the peak of the X-ray emission and in other two regions of the galaxy,

concluding that it is not enough to explain the observed He II emission. Accordingly, this implies that the ULX cannot explain [O IV] as well as [Ne V] emission.

### 5.2.3. Shocks

Shocks models are generally considered an important source of ionization in MIR diagnostic diagrams and can be due to several phenomena, including cloud-cloud collisions, the expansion of H II regions, outflows and/or supernovae (e.g., [Groves et al. 2004](#)). Given the disturbed kinematic of this galaxy (Fig. 7; see also [Izotov et al. 2006; Herenz et al. 2023](#)), the presence of clear shells in the H $\alpha$  and He II morphology ([Herenz et al. 2017; Kehrig et al. 2018](#)) as well as diffuse non-thermal radio emission interpreted as an ensemble of compact supernova remnants expanding in a dense ISM ([Hunt et al. 2004](#)), it is plausible that shocks are present and can play an important role. Unfortunately, the shell structure clearly visible in the He II morphology is not covered in our MIRI/MRS observations. This region is slightly north-west to the area where we see  $\sim 50$  km/s red-shifted velocities and intrinsic velocity dispersion enhancement in [S IV] and [Ne III] (Fig. 7).

Having said that, as shown in Figs. 8, 13 and 14, low-metallicity [F24](#) (and also [AM19](#), not shown) shock models do not overlap with our data. The grids could match the range of observed [O IV]/[Ne III], but cannot explain the corresponding [Ne V]/[Ne II], [Ne III]/[Ne II] and [S IV]/[Ne II] line ratios. Another hint towards shocks not being the primary source of ionization of the extended [O IV] and [Ne V] emission is the complete lack of co-spatial [Fe II] emission (see Sec. 5.1). Finally, [Kehrig et al. \(2018\)](#) also excluded shocks as the cause of the He II emission, given the lack of high  $S/N$  ([O I]  $\lambda 6300$ ) and lack of low [S II]/H $\alpha$  line ratios, generally considered to be good shock indicators (e.g., [Kewley et al. 2019; Mingozi et al. 2024](#)).

There might be other factors to consider when explaining the misalignment of shock models and extended high ionization emission. First, shock fronts have spatial scales much below our spatial resolution (down to  $\sim 10$  pc; [Calzetti et al. 2004](#)), which could dilute shock-driven line ratios with other ionizing sources when integrating over spatial scales larger than a shock front. Second, it is possible that new shock models with an updated treatment of the radiative transfer with respect to Mappings V could be in better agreement with our data (e.g., [Godard et al. 2024](#)). However, these new models have not been tested yet at low-metallicity and currently take into account only velocities below 500 km/s. Overall, we cannot completely exclude the presence of shocks, but according to the available model predictions, they do not represent the main source of ionization of MIR lines in SBS 0335-052 E.

### 5.2.4. The possibility of an IMBH

Recent works have suggested the presence of a  $10^3 - 10^5 M_{\odot}$  IMBH in SBS 0335-052 E, due to the detection of [Ne V]  $\lambda 3426$  (Hatano et al. 2024), as well as possible variability in NEOWISE data ( $3 - 4 \mu\text{m}$ ) over 12 years (Hatano et al. 2023). Interestingly, the [Ne V]  $\lambda 3426$  was first observed by Thuan & Izotov 2005 and does not show any sign of variability (Hatano et al. 2024). Hatano et al. (2023) proposed also the presence of broad  $H\alpha$  emission possibly due to the BH broad line region, from which they estimate a  $M_{BH} \sim 10^8 M_{\odot}$  upper limit. However, this value is much larger than the mass of the different components of this galaxy (see Tab. 2), raising doubts that this emission is tracing the BH broad line region (see also Sec. 5.3), unless the system is not virialized (e.g., Bertemes et al. 2025). As such, the existence of [Ne V]  $\lambda 3426$  and the observed NIR variability seem the two most feasible clues from the literature to suggest the presence of an IMBH in SBS 0335-052 E.

In consideration of these suggestions of an IMBH, looking at Fig. 8 and Fig. 13, the models that uniquely cover the observed [Ne V]/[Ne II], [Ne III]/[Ne II] and [S IV]/[Ne II] line ratios that we measure in SBS 0335-052 E are the  $M_{BH} = 10^5 M_{\odot}$  IMBH models from R22 with an AGN fraction 4-8-16% and  $\log(U)$  between  $-2$  and  $-0.5$  (the closed geometry model can better reach the highest [Ne III]/[Ne II]). According to the R22 models, we can exclude the possibility of a BH with  $M_{BH} = 10^3 M_{\odot}$  because this BH mass would imply too low  $\log([Ne III]/[Ne II]) (\leq 0.5)$  and  $\log([Ne V]/[Ne II]) (\leq 0)$  with respect to the observed data, regardless of the other parameter selection (i.e., AGN fraction, geometry, gas density, stellar age). We can also exclude R22  $M_{BH} = 10^4 M_{\odot}$  grids, which still cannot reach the  $\log([Ne V]/[Ne II])$  values that we observe ( $\leq 0.3$ ). R22  $M_{BH} = 10^6 M_{\odot}$  can overlap with the observed [Ne V]/[Ne II] vs [Ne III]/[Ne II] at 8% AGN fraction, but at lower/higher fractions, they predict larger/lower [Ne III]/[Ne II] than what we observe.

A great advantage of the MIRI/MRS data is that we can spatially resolve line ratios and trace the ionization hardness (e.g., [Ne V]/[Ne II], [O IV]/[Ne III]), finding their peak around/north SSCs 4,5 and S7 and with decreasing values towards south-east (see Fig. 6). As already discussed in Sec. 4.3, this peak region is characterized by the most disturbed kinematics with the presence of gas flows (Fig. 7; see also Izotov et al. 2006; Herenz et al. 2023). In particular, the [S IV], [Ne III] and [Ne V] intrinsic velocity dispersion maps revealed an interesting “V shape” in the north-west region, starting at the position of SSCs 4-5, high-resolution optical IFU data revealed doubled-peak  $H\alpha$  and He II profiles, suggesting the presence of an expanding shell (Izotov et al. 2006). In this scenario, SSC5 may correspond to the location of the IMBH. Another potentially relevant element is that SSC5 is also found to have a very compact ( $< 10$  pc)

NIR emitting region not resolved in HST NICMOS (high resolution,  $0.075''/\text{px}$ ) data (Thompson et al. 2009).

However, we do stress that even the R22 models do not perfectly overlap with our data, since they are not able to reproduce the combination of highest [O IV]/[Ne III] and [Ne III]/[Ne II] values (see Fig. 14). Many factors could be at play here with regards to the assumptions and parameters held within the models - each of which are difficult to constrain with observations alone due to the degeneracies between them. For instance, R22 predictions can vary as a function of the considered SEDs (R22 considered two extreme values, qso or disk-plaw) and assumptions on accretion rate and spin (incorporated as fixed parameters in the qso SED), as well as the choice of geometry (open vs closed). Also, we stress that [O IV]/[Ne III] can be affected by the wavelength-dependent MIRI/MRS PSF variation correction, as well as residual fringing (see Sec. 4.4).

### 5.3. Implications for high- $z$ galaxies and UV-optical diagnostics

An unexpectedly large population of objects with possible accreting black holes has started to be revealed at high- $z$  ( $z \sim 6 - 12$ ) with masses up to  $M \sim 10^8 M_{\odot}$  (e.g., Furtak et al. 2023; Harikane et al. 2023; Labbé et al. 2023; Scholtz et al. 2023; Larson et al. 2023; Greene et al. 2024; Greene & Ho 2004; Maiolino et al. 2023a; Kokorev et al. 2024; Chisholm et al. 2024; Hayes et al. 2024; Cammelli et al. 2025; as introduced in Sec. 1). Not only has this led to questions concerning their rapid formation (in just  $\sim 300$  Myr) and their subsequent impact on galaxy evolution, but also opened up discussions on which methods can unambiguously identify them.

As previously mentioned, one of the most popular criteria to identify AGN activity so far has been via broad permitted emission lines (e.g.,  $H\alpha$ ). From a visual inspection of VLT/MUSE observations of SBS 0335-052 E MUSE, it appears that a broad  $H\alpha$  profile exists at both the position of cluster SSC1 (i.e., the MIR point source with no clear [Ne V] detection) and at the peak of He II, [Ne V], and UV emission, with FWHM up to  $\sim 1200$  km/s (see Fig. 15 and App. C). In particular, both the  $H\alpha$  and [O III]  $\lambda 5007$  emission lines require up to 3-4 Gaussian components to be well fitted, with also [O III]  $\lambda 5007$  showing a fainter broad (up to FWHM  $\sim 900$  km/s) component. Interestingly, broad  $H\alpha$  and the need of  $> 2$  components to reproduce the kinematics of the ionized gas has also been noticed in other nearby BCDs (e.g., James et al. 2009; del Valle-Espinosa et al. 2023; Komarova et al. 2021) and other high- $z$  analogs (e.g., Green Peas; Amorín et al. 2024), with interpretations ranging from turbulent mixing layers, high-density gas, and radiatively driven winds. Despite the origin of this broadening still not being completely understood in these systems, there could be

a connection with (some of) the broad-line galaxies revealed at high- $z$ .

Exploiting the use of high- $z$  analogs, Mingozi et al. (2024) used optical and UV spectra from the Cosmic Origins Spectrograph (COS) Legacy Archive Spectroscopic Survey (CLASSY; Berg et al. 2022; James et al. 2022) to provide a toolkit to distinguish star formation and AGN activity at high- $z$ . In particular, CLASSY is a treasury of 45 nearby ( $0.002 < z < 0.182$ ) star-forming galaxies, including SBS 0335-052 E, generally characterized by lower stellar masses, higher SFRs and more extreme ionization fields than  $z \sim 0$  objects, as typically observed in the EoR. Specifically, Mingozi et al. (2024) proposed the C III]  $\lambda\lambda 1907,9$ /He II  $\lambda 1640$  versus O III]  $\lambda 1666$ /He II  $\lambda 1640$  as the most reliable UV diagnostic diagram (their Fig. 6), being capable of separating the SF, AGN and shocks at low-metallicity. We re-propose this diagnostic diagram in Fig. 9, showing the CLASSY sample compared with R22 models with the same parameters presented in Figure 8 and discussed in Section 5.2.4. The fact that SBS 0335-052 E (light-pink square) lies very close to the line separators was interpreted by Mingozi et al. (2024) as being due a combination of its low-metallicity environment and hard stellar radiation field. However, the R22  $M_{BH} = 10^5 M_{\odot}$  IMBH model with 8% AGN fraction at the lowest metallicity and highest  $\log(U)$  would also explain the UV line ratios observed in SBS 0335-052 E. Since the UV emission line fluxes are from spectra integrated over the COS aperture ( $2.5''$ ; see Fig. 1) covering the [Ne V]  $\lambda 14.3$  emitting region, the fact that the UV line ratios can be reproduced by the same set of models that explain part of the spatially resolved MIR line ratios indeed strengthens the validity of the R22 models in describing this object. This finding also highlights a previously unknown degeneracy of this diagnostic diagram in distinguishing between pure star-forming objects and objects with an AGN fraction  $\sim 4-8\%$  (when considering R22 models).

The MIR wavelength range is not observable in high- $z$  targets, but JWST does provide coverage of [Ne V]  $\lambda 3426$  in the optical wavelength range (e.g., Cleri et al. 2023; Scholtz et al. 2023; Chisholm et al. 2024). As mentioned at the beginning of Sec. 5, optical [Ne V] has been revealed in a few nearby BCDs, including SBS 0335-052 E. Thus, it is interesting to see how SBS 0335-052 E compares to other BCDs and high- $z$  targets within which this emission has been observed. In Fig. 10 we show the diagnostic diagram He II  $\lambda 4686/H\beta$  vs [Ne V]  $\lambda 3426/[Ne III] \lambda 3868$  proposed by Chisholm et al. (2024) to identify the presence of accreting IMBHs. Indeed, similarly to the MIR line ratios explored in Fig. 8, both [Ne V]/[Ne III] and He II/ $H\beta$  are relatively insensitive to metallicity and instead trace the ionization parameter and the radiation hardness (Shirazi & Brinchmann 2012; Cleri et al. 2023; Chisholm et al. 2024). Consistently

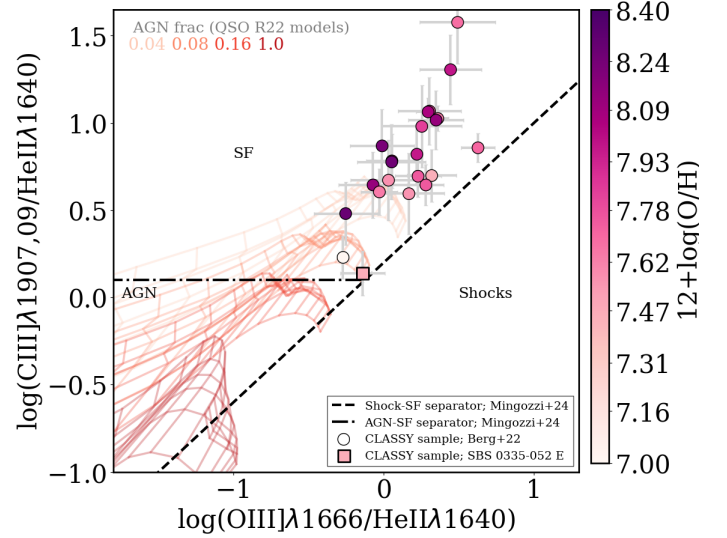


**Figure 9.** C III]  $\lambda\lambda 1907,9$ /He II  $\lambda 1640$  versus O III]  $\lambda 1666$ /He II  $\lambda 1640$  UV diagnostic diagram, showing SBS 0335-052 E as well as other nearby high- $z$  analogs from the CLASSY survey (Berg et al. 2022; James et al. 2022), color-coded as function of gas-phase metallicity. The models superimposed are the R22 models that best-reproduced the MIR line ratios, thus enabling us to assess how the model UV line ratios behave within a metallicity range consistent with the CLASSY sample. This UV-based diagnostic diagram is the best in discriminating SF, AGN and shocks at sub-solar metallicities according to Mingozi et al. (2024). SBS 0335-052 E UV line ratios, falling in the SF locus, are also consistent with the R22 models with  $M_{BH} = 10^5 M_{\odot}$  and 8% AGN fraction, that reproduced the MIR line ratios. Regardless of this degeneracy, this diagram should still be regarded as an important tool in classifying the ionization source of galaxies based on their UV line ratios.

with the MIR (Fig. 8) and UV line ratios (Fig. 9), SBS 0335-052 E's optical line ratios are also consistent with the R22  $M_{BH} = 10^5 M_{\odot}$  IMBH models with 8% AGN fraction. Interestingly, SBS 0335-052 E's [Ne V]/[Ne III] flux ratio (pink square) is below the median values found for the 13 currently known nearby BCD [Ne V] emitters (Izotov et al. 2004; 2012; 2021; Thuan & Izotov 2005) and is  $\sim 1/9$  of the value found for the  $z \sim 5.59$  galaxy studied by Chisholm et al. (2024).

Upon reflection of our comparison with UV and optical emission line diagnostics, our analysis suggests that the MIR high-ionization emission that we observe in SBS 0335-052 E could indeed be powered by an accreting IMBH. According to the best-fitting R22 models, the mass of the IMBH would be  $M_{BH} = 10^5 M_{\odot}$ , placing it slightly above the scaling relation between  $M_{BH}$  and the host galaxy stellar mass, as seen for many objects at high- $z$  (e.g., Maiolino et al. 2023a). However, given the fact that there are several open questions regarding the predicted high-ionization emission of other models, alternative sources of ionization cannot be ruled out. In particular, it is not clear if we have completely understood the

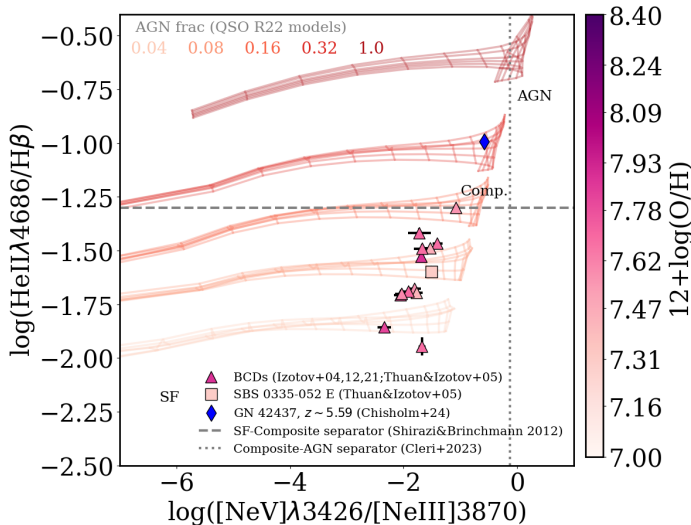


**Figure 10.** He II  $\lambda 4686/H\beta$  vs [Ne V]  $\lambda 3426/[Ne III] \lambda 3868$  emission-line diagnostic diagram, recently proposed by Chisholm et al. (2024) to probe the strength of very high-ionization emission lines independently of gas-phase metallicity. The square shows SBS 0335-052 E line ratios (Thuan & Izotov 2005), while the dots show the currently known BCDs showing optical [Ne V] emission (i.e., 14, including SBS 0335-052 E; Izotov et al. 2004; Thuan & Izotov 2005; Izotov et al. 2012; 2021). The blue diamond is the galaxy at  $z \sim 5.59$  found by Chisholm et al. (2024), to put SBS 0335-052 E and BCDs in the high- $z$  context. The dashed and dotted lines show the separators proposed by Shirazi & Brinchmann (2012) and Cleri et al. (2023) to distinguish SF and composite, and composite and AGN, respectively.

atmosphere of low metallicity massive stars (see Sec. 5.2.1), or how to constrain the different parameters within X-ray binaries, shocks and IMBHs models (see Sec. 5.2.2, Sec. 5.2.3, Sec. 5.2.4). As such, our model-based conclusions can only be as firm as the models are realistic.

## 6. CONCLUSIONS

In this paper, we reported the first JWST MIRI/MRS data of a BCD, focusing on the galaxy SBS 0335-052 E. This object is well-known for its extremely metal-poor environment, complex kinematics, high-ionization optical and UV emission lines, and the possible presence of an IMBH, which makes it the perfect analog of high- $z$  systems in the EoR. In particular, we used MIRI/MRS data to spatially resolve the MIR emission in this BCD (down to  $\sim 0.4 - 0.9''$ ,  $\sim 112 - 252$  pc) through emission lines tracing different levels of ionization (e.g., [Ne II], [S IV], [Ne III], [O IV], [Ne V]) of the ionized gas. In this way, we can reveal the ionization structure of this galaxy and investigate the possible accreting IMBH or other non-stellar ionizing sources, building on the many previous works carried out since SBS 0335-052 E discovery (Izotov et al. 1990). In the following, we summarize our main findings:

- We revealed the presence of a point-source-like emission dominating the continuum and emission-line fluxes close to the position of one of the youngest and most embedded stellar clusters, SSC1 ( $t \sim 3$  Myr,  $A_V \sim 20$ ; see Fig. 1). We accurately modeled and isolated its emission (see Fig. 2; Sec. A), to study in detail its properties as well as the underlying extended emission. The point-source spectrum does not show very high-ionization emission (i.e., [Ne V]  $\lambda 14.32$ ), and is characterized by the strongest silicate feature at  $9.7 \mu\text{m}$ ,  $H_2$  molecular gas emission and low ionization lines (i.e., [Fe II]  $\lambda 5.34$ ). As we discuss in Sec. 5.1, there is not a straightforward explanation to explain all its characteristics. R22  $M_{BH} = 10^5 M_\odot$  IMBH models can well reproduce the detected MIR lines, but cannot explain the low [Ne V]/[Ne II] upper limit.
- We revealed extended high ionization emission lines such as [O IV]  $\lambda 25.89$  and [Ne V]  $\lambda 14.32$ , localized mainly in the north-west region of the galaxy, covering SSCs 3-4-5-6 and S7 (all older than the point source SSC1). In particular, this is the first [Ne V]  $\lambda 14.32$  detection in a BCD (Sec. 4.1, Fig. 5).
- We spatially resolved line ratios tracing the ionization hardness (e.g., [Ne V]/[Ne II], [O IV]/[Ne III]), finding their peak around/north SSCs 4,5 and S7 and with decreasing values towards south-east (Sec. 4.2, Fig. 6). Interestingly, we found  $\log([Ne V]/[Ne II]) > 0$ , higher than any upper limit proposed for BCDs with previous IR telescopes (Sec. 4.2, Fig. 6).
- We showed how the region at the peak of the ionization hardness is characterized by the most disturbed kinematics with the presence of gas flows and enhanced velocity dispersion, consistent with the presence of an expanding shell as suggested in previous works (Sec. 4.3; Fig. 7).
- We explored MIR diagnostic diagrams, comparing MIR line ratios with a set of state-of-the-art photoionization and shock models, finding that SBS 0335-052 E lies outside of the “canonical” SF locus and can be best reproduced by R22  $n_H = 100 \text{ cm}^{-3}$   $M_{BH} = 10^5 M_\odot$  IMBH models with AGN fraction  $< 16\%$  (Sec. 4.4; Fig. 8, Fig. 13). However, these models struggle to reproduce the highest [O IV]/[Ne III] MIR line ratios (Fig. 14).
- The R22 models are consistent also with UV and optical emission-line diagnostics (Sec. 5.3; Fig. 9, Fig. 10), strengthening the possibility of the presence of an accreting IMBH. On the other hand, star-forming models (regardless of including X-ray binaries) and shocks

struggle to reproduce even MIR line ratios tracing lower ionization than [O IV] and [Ne V] (Fig. 13), typically observed in BCDs, suggesting possible model limitations. In Sec. 5.2 (see also 5.3) we also highlight how there are several open questions regarding the predicted high-ionization emission of other models, implying that alternative sources of ionization (e.g., very massive stars, Sec. 5.2.1; Ultra Luminous X-ray sources, Sec. 5.2.2; shocks, Sec. 5.2.3) cannot be completely ruled out.

Overall, until models are adapted to fully replicate the ionizing sources, one way to step-forward in our understanding of the role that objects such as SBS 0335-052 E have in interpreting the high- $z$  universe would be to perform detailed multi-wavelength modelling, i.e. utilizing the full X-ray–sub-mm information as constraints. Finding more near and far [Ne V] emitters, as well as investigating more dwarf AGN candidates (e.g., Polimera et al. 2022; Mezcuca & Domínguez Sánchez 2024; Wasleske & Baldassare 2024), covering a diverse range of properties, will also help to better understand the conditions required to produce this high-ionization emission.

This research is based on observations made with the NASA/ESA Hubble Space Telescope obtained from the

Space Telescope Science Institute, which is operated by the Association of Universities for Research in Astronomy, Inc., under NASA contract NAS 5–26555. These observations are associated with program JWST-4278. MM, BLJ and SH are thankful for support from the European Space Agency (ESA). MJH is supported by the Swedish Research Council (Vetenskapsradet), and is fellow of the Knut & Alice Wallenberg Foundation. RA acknowledges the support of project PID2023-147386NB-I00 and the Severo Ochoa grant CEX2021-001131-S funded by MCIN/AEI/10.13039/50110001103. This research has used the HSLA database, developed and maintained at STScI, Baltimore, USA. MM is grateful to Carlo Cannarozzo for inspiring conversations and advice.

*Facilities:* JWST (MIRI), HST (COS, ACS), VLT (MUSE)

*Software:* astropy (The Astropy Collaboration 2013, 2018) dustmaps (Green 2018), jupyter (Kluyver 2016), LINMIX (Kelly 2007) Photutils (Bradley 2021), python, pysynphot (STScI Development Team)

## REFERENCES

- Abel, N. P., & Satyapal, S. 2008, *ApJ*, 678, 686
- Adamo, A., Zackrisson, E., Östlin, G., & Hayes, M. 2010, *ApJ*, 725, 1620
- Alarie, A., & Morisset, C. 2019, *RMxAA*, 55, 377
- Allen, M. G., Groves, B. A., Dopita, M. A., Sutherland, R. S., & Kewley, L. J. 2008, *ApJS*, 178, 20
- Álvarez-Márquez, J., Crespo Gómez, A., Colina, L., et al. 2024, *arXiv e-prints*, [arXiv:2412.12826](https://arxiv.org/abs/2412.12826)
- Amorín, R. O., Rodríguez-Henríquez, M., Fernández, V., et al. 2024, *A&A*, 682, L25
- Asplund, M., Grevesse, N., Sauval, A. J., & Scott, P. 2009, *ARA&A*, 47, 481
- Atek, H., Labbé, I., Furtak, L. J., et al. 2024, *Nature*, 626, 975
- Backhaus, B. E., Trump, J. R., Pirzkal, N., et al. 2024, *ApJ*, 962, 195
- Bagley, M. B., Finkelstein, S. L., Koekemoer, A. M., et al. 2023, *ApJL*, 946, L12
- Berg, D. A., Chisholm, J., Erb, D. K., et al. 2019, *ApJL*, 878, L3
- . 2021, *ApJ*, 922, 170
- Berg, D. A., James, B. L., King, T., et al. 2022, *ApJS*, 261, 31
- Bertemes, C., Wylezalek, D., Rupke, D. S. N., et al. 2025, *A&A*, 693, A176
- Bezanson, R., Labbe, I., Whitaker, K. E., et al. 2024, *ApJ*, 974, 92
- Brinchmann, J. 2023, *MNRAS*, 525, 2087
- Brown, T. M., Smith, E., Ferguson, H. C., et al. 2008, *ApJ*, 682, 319
- Bruzual, G., & Charlot, S. 2003, *MNRAS*, 344, 1000
- Bunker, A. J., Cameron, A. J., Curtis-Lake, E., et al. 2023, *arXiv e-prints*, [arXiv:2306.02467](https://arxiv.org/abs/2306.02467)
- Calzetti, D., Harris, J., Gallagher, III, J. S., et al. 2004, *AJ*, 127, 1405
- Cammelli, V., Tan, J. C., Young, A. R., et al. 2025, *arXiv e-prints*, [arXiv:2501.17675](https://arxiv.org/abs/2501.17675)
- Carniani, S., Hainline, K., D’Eugenio, F., et al. 2024a, *Nature*, 633, 318
- Carniani, S., Venturi, G., Parlanti, E., et al. 2024b, *A&A*, 685, A99
- Castellano, M., Napolitano, L., Fontana, A., et al. 2024, *ApJ*, 972, 143
- Chisholm, J., Berg, D. A., Endsley, R., et al. 2024, *MNRAS*, 534, 2633
- Cleri, N. J., Olivier, G. M., Hutchison, T. A., et al. 2023, *ApJ*, 953, 10
- Dasyra, K. M., Paraschos, G. F., Combes, F., et al. 2024, *ApJ*, 977, 156

- Dayal, P., Volonteri, M., Greene, J. E., et al. 2024, arXiv e-prints, arXiv:2401.11242
- del Valle-Espinosa, M. G., Sánchez-Janssen, R., Amorín, R., et al. 2023, MNRAS, 522, 2089
- Eldridge, J. J., Stanway, E. R., Xiao, L., McClelland, L. A. S., & others. 2017, PASA, 34, e058
- Feltre, A., Charlot, S., & Gutkin, J. 2016, MNRAS, 456, 3354
- Ferland, G. J., Chatzikos, M., Guzmán, F., et al. 2017, RMxAA, 53, 385
- Fernández-Ontiveros, J. A., Spinoglio, L., Pereira-Santaella, M., et al. 2016, ApJS, 226, 19
- Flury, S. R., Arellano-Córdova, K. Z., Moran, E. C., & Einsig, A. 2024, arXiv e-prints, arXiv:2412.06763
- Fragos, T., Lehmer, B., Tremmel, M., et al. 2013, ApJ, 764, 41
- Furtak, L. J., Zitrin, A., Plat, A., et al. 2023, ApJ, 952, 142
- Garofali, K., Basu-Zych, A. R., Johnson, B. D., et al. 2024, ApJ, 960, 13
- Godard, B., des Forêts, G. P., & Bialy, S. 2024, A&A, 688, A169
- Goold, K., Seth, A., Molina, M., et al. 2024, ApJ, 966, 204
- Gordon, K. D., Clayton, G. C., Declair, M., et al. 2023, ApJ, 950, 86
- Greene, J. E., & Ho, L. C. 2004, ApJ, 610, 722
- Greene, J. E., Strader, J., & Ho, L. C. 2020, ARA&A, 58, 257
- Greene, J. E., Labbe, I., Goulding, A. D., et al. 2024, ApJ, 964, 39
- Groves, B., Nefs, B., & Brandl, B. 2008, MNRAS, 391, L113
- Groves, B. A., Dopita, M. A., & Sutherland, R. S. 2004, ApJS, 153, 75
- Hao, L., Wu, Y., Charmandaris, V., et al. 2009, ApJ, 704, 1159
- Harikane, Y., Zhang, Y., Nakajima, K., et al. 2023, ApJ, 959, 39
- Hatano, S., Ouchi, M., Nakajima, K., et al. 2023, arXiv e-prints, arXiv:2304.03726
- Hatano, S., Ouchi, M., Umeda, H., et al. 2024, ApJ, 966, 170
- Hayes, M. J., Tan, J. C., Ellis, R. S., et al. 2024, ApJL, 971, L16
- Herenz, E. C., Hayes, M., Papaderos, P., et al. 2017, A&A, 606, L11
- Herenz, E. C., Micheva, G., Weilbacher, P. M., et al. 2023, Research Notes of the AAS, 7, 99. <https://dx.doi.org/10.3847/2515-5172/acd69e>
- Houck, J. R., Charmandaris, V., Brandl, B. R., et al. 2004, ApJS, 154, 211
- Hunt, L. K., Dyer, K. K., Thuan, T. X., & Ulvestad, J. S. 2004, ApJ, 606, 853
- Hunt, L. K., Vanzi, L., & Thuan, T. X. 2001, A&A, 377, 66
- Hunt, L. K., Testi, L., Casasola, V., et al. 2014, A&A, 561, A49
- Inami, H., Armus, L., Charmandaris, V., et al. 2013, ApJ, 777, 156
- Izotov, I. I., Guseva, N. G., Lipovetskii, V. A., Kniazev, A. I., & Stepanian, J. A. 1990, Nature, 343, 238
- Izotov, Y. I., Lipovetsky, V. A., Chaffee, F. H., et al. 1997, ApJ, 476, 698
- Izotov, Y. I., Noeske, K. G., Guseva, N. G., et al. 2004, A&A, 415, L27
- Izotov, Y. I., Schaerer, D., Blecha, A., et al. 2006, A&A, 459, 71
- Izotov, Y. I., Thuan, T. X., & Guseva, N. G. 2021, MNRAS, 508, 2556
- Izotov, Y. I., Thuan, T. X., & Privon, G. 2012, MNRAS, 427, 1229
- James, B. L., Tsamis, Y. G., Barlow, M. J., et al. 2009, MNRAS, 398, 2
- James, B. L., Berg, D. A., King, T., et al. 2022, ApJS, 262, 37
- Johnson, K. E., Hunt, L. K., & Reines, A. E. 2009, AJ, 137, 3788
- Jones, L. H., Hernandez, S., Smith, L. J., et al. 2024, arXiv e-prints, arXiv:2410.09020
- Jones, O. C., Álvarez-Márquez, J., Sloan, G. C., et al. 2023, MNRAS, 523, 2519
- Juod vzbališ, I., Maiolino, R., Baker, W. M., et al. 2024, Nature, 636, 594
- Kehrig, C., Vílchez, J. M., Guerrero, M. A., & others. 2018, MNRAS, 480, 1081
- Kewley, L. J., Nicholls, D. C., & Sutherland, R. S. 2019, ARA&A, 57, 511
- Kocevski, D. D., Finkelstein, S. L., Barro, G., et al. 2024, arXiv e-prints, arXiv:2404.03576
- Kokorev, V., Fujimoto, S., Labbe, I., et al. 2023, ApJL, 957, L7
- Kokorev, V., Caputi, K. I., Greene, J. E., et al. 2024, arXiv e-prints, arXiv:2401.09981
- Komarova, L., Oey, M. S., Krumholz, M. R., et al. 2021, ApJL, 920, L46
- Koo, B.-C., Raymond, J. C., & Kim, H.-J. 2016, Journal of Korean Astronomical Society, 49, 109
- Kroupa, P. 2001, MNRAS, 322, 231
- Kumari, N., Smit, R., Leitherer, C., et al. 2024, MNRAS, 529, 781
- Labbe, I., van Dokkum, P., Nelson, E., et al. 2023, Nature, 616, 266
- Larson, R. L., Finkelstein, S. L., Kocevski, D. D., et al. 2023, ApJL, 953, L29
- Law, D. R., E. Morrison, J., Argyriou, I., et al. 2023, AJ, 166, 45
- Leitherer, C., Schaerer, D., Goldader, J. D., et al. 1999, ApJS, 123, 3
- Maiolino, R., Scholtz, J., Curtis-Lake, E., et al. 2023a, arXiv e-prints, arXiv:2308.01230
- Maiolino, R., Scholtz, J., Witstok, J., et al. 2023b, arXiv e-prints, arXiv:2305.12492
- Mapelli, M., Ripamonti, E., Zampieri, L., & Colpi, M. 2011, Astronomische Nachrichten, 332, 414
- Mapelli, M., Ripamonti, E., Zampieri, L., Colpi, M., & Bressan, A. 2010, MNRAS, 408, 234
- Marshall, J. A., Herter, T. L., Armus, L., et al. 2007, ApJ, 670, 129
- Martin, C. L., Peng, Z., & Li, Y. 2024, ApJ, 966, 190
- Martínez-Paredes, M., Bruzual, G., Morisset, C., et al. 2023, MNRAS, 525, 2916
- Matthee, J., Naidu, R. P., Brammer, G., et al. 2024, ApJ, 963, 129

- Mezcua, M., & Domínguez Sánchez, H. 2024, *MNRAS*, 528, 5252
- Mignoli, M., Vignali, C., Gilli, R., et al. 2013, *A&A*, 556, A29
- Mingozzi, M., James, B. L., Arellano-Córdova, K. Z., et al. 2022, *ApJ*, 939, 110
- Mingozzi, M., James, B. L., Berg, D. A., et al. 2024, *ApJ*, 962, 95
- Moiseev, A. V., Pustilnik, S. A., & Kniazev, A. Y. 2010, *MNRAS*, 405, 2453
- Nakajima, K., Ouchi, M., Isobe, Y., et al. 2024, arXiv e-prints, arXiv:2412.04541
- Papaderos, P., Izotov, Y. I., Fricke, K. J., Thuan, T. X., & Guseva, N. G. 1998, *A&A*, 338, 43
- Papaderos, P., Izotov, Y. I., Guseva, N. G., Thuan, T. X., & Fricke, K. J. 2006, *A&A*, 454, 119
- Parker, K. S., Berg, D. A., Gazagnes, S., et al. 2024, *ApJ*, 977, 104
- Perrin, M. D., Sivaramakrishnan, A., Lajoie, C.-P., et al. 2014, in *Society of Photo-Optical Instrumentation Engineers (SPIE) Conference Series*, Vol. 9143, *Space Telescopes and Instrumentation 2014: Optical, Infrared, and Millimeter Wave*, ed. J. M. Oschmann, Jr., M. Clampin, G. G. Fazio, & H. A. MacEwen, 91433X
- Plante, S., & Sauvage, M. 2002, *AJ*, 124, 1995
- Plat, A., Charlot, S., Bruzual, G., et al. 2019, *MNRAS*, 490, 978
- Polimera, M. S., Kannappan, S. J., Richardson, C. T., et al. 2022, *ApJ*, 931, 44
- Prestwich, A. H., Tsantaki, M., Zezas, A., et al. 2013, *ApJ*, 769, 92
- Reines, A. E., Johnson, K. E., & Hunt, L. K. 2008, *AJ*, 136, 1415
- Rémy-Ruyer, A., Madden, S. C., Galliano, F., et al. 2015, *A&A*, 582, A121
- Richardson, C. T., Simpson, C., Polimera, M. S., et al. 2022, *ApJ*, 927, 165
- Robertson, B. E., Ellis, R. S., Furlanetto, S. R., & Dunlop, J. S. 2015, *ApJL*, 802, L19
- Roy, A., Krumholz, M. R., Salvadori, S., et al. 2025, arXiv e-prints, arXiv:2501.08376
- Sander, A. A. C. 2022, arXiv e-prints, arXiv:2211.05424
- Schaerer, D., Marques-Chaves, R., Barrufet, L., et al. 2022, *A&A*, 665, L4
- Schaerer, D., & Vacca, W. D. 1998, *ApJ*, 497, 618
- Scholtz, J., Maiolino, R., D'Eugenio, F., et al. 2023, arXiv e-prints, arXiv:2311.18731
- Senchyna, P., Plat, A., Stark, D. P., & Rudie, G. C. 2023, arXiv e-prints, arXiv:2303.04179
- Senchyna, P., Stark, D. P., Charlot, S., et al. 2021, *MNRAS*, 503, 6112
- Shirazi, M., & Brinchmann, J. 2012, *MNRAS*, 421, 1043
- Simmonds, C., Tacchella, S., Hainline, K., et al. 2024, *MNRAS*, 527, 6139
- Stanway, E. R., Eldridge, J. J., & Becker, G. D. 2016, *MNRAS*, 456, 485
- Stark, D. P., Richard, J., Charlot, S., & others. 2015, *MNRAS*, 450, 1846
- Stasińska, G., Vale Asari, N., Cid Fernandes, R., et al. 2008, *MNRAS*, 391, L29
- Sutherland, R. S., & Dopita, M. A. 2017, *ApJS*, 229, 34
- Telford, O. G., McQuinn, K. B. W., Chisholm, J., & Berg, D. A. 2023, *ApJ*, 943, 65
- Thompson, R. I., Sauvage, M., Kennicutt, R. C., et al. 2009, *ApJ*, 691, 1068
- Thuan, T. X., Bauer, F. E., Papaderos, P., & Izotov, Y. I. 2004, *ApJ*, 606, 213
- Thuan, T. X., & Izotov, Y. I. 2005, *ApJS*, 161, 240
- Thuan, T. X., Izotov, Y. I., & Lipovetsky, V. A. 1997, *ApJ*, 477, 661
- Topping, M. W., Stark, D. P., Senchyna, P., et al. 2024, *MNRAS*, 529, 3301
- Übler, H., Maiolino, R., Curtis-Lake, E., et al. 2023, arXiv e-prints, arXiv:2302.06647
- Übler, H., Maiolino, R., Pérez-González, P. G., et al. 2024, *MNRAS*, 531, 355
- Vink, J. S. 2012, in *IAU Symposium*, Vol. 279, *Death of Massive Stars: Supernovae and Gamma-Ray Bursts*, ed. P. Roming, N. Kawai, & E. Pian, 29–33
- Wasleske, E. J., & Baldassare, V. F. 2024, *ApJ*, 971, 68
- Weaver, K. A., Meléndez, M., Mushotzky, R. F., et al. 2010, *ApJ*, 716, 1151
- Wise, J. H., Demchenko, V. G., Halicek, M. T., et al. 2014, *MNRAS*, 442, 2560
- Wofford, A., Vidal-García, A., Feltre, A., Chevallard, J., et al. 2021, *MNRAS*, 500, 2908
- Xiao, L., Stanway, E. R., & Eldridge, J. J. 2018, *MNRAS*, 477, 904
- Xu, X., Heckman, T., Henry, A., et al. 2022, *ApJ*, 933, 222



## APPENDIX

## A. POINT SOURCE SUBTRACTION PROCEDURE

We modelled the PSF for each MIRI/MRS band using v 1.4.0 WebbPSF (Perrin et al. 2014) and the function *calc\_datacube*<sup>4</sup>, taking into account the same native pixel scale and spectral binning of the observed data. We created the pipeline Stage 3 products by band, selecting the option *ifualign*, to have them aligned with the WebbPSF models. Then, we extracted  $1 \mu\text{m}$  ( $1.5 \mu\text{m}$  for Channel 4) slices around the emission lines taken into account in this paper (see Sec. 3.1) from the Stage 3 band datacubes. We localized the point source position in each slice, modeling a 2D Gaussian distribution in a region of the spectrum with solely continuum emission, where the point-source structure is more enhanced (emission lines have also extended emission). Then, using photutils PSFphotometry we found the best-fit model of the point-source emission in each slice, wavelength-by-wavelength, putting very tight constraints on its position and allowing the PSF model normalization to vary to match the flux in a region  $\sim 2$  times the PSF FWHM. According to WebbPSF and JWST documentation, the PSF FWHM in Channel 1, 2, 3 and 4 is  $\sim 0.4''$ ,  $0.5''$ ,  $0.6''$ ,  $0.9''$  (i.e., 2, 2.5, 3, 4.5 px), respectively.

Fig 11 displays an example of the data, the original WebbPSF model, the best-fit model we find with photutils and the residual extended emission for one wavelength close to the [Ne III]  $\lambda 15.56$  emission, where both point-like source and extended emission are clearly visible (see upper left panel). The lack of PSF structure in the residual map and the good match between the radial distributions within  $\sim 3$  px from the point source location (Channel 3C PSF FWHM  $\sim 0.6'' \sim 3$  px) validate our point-source subtraction procedure.

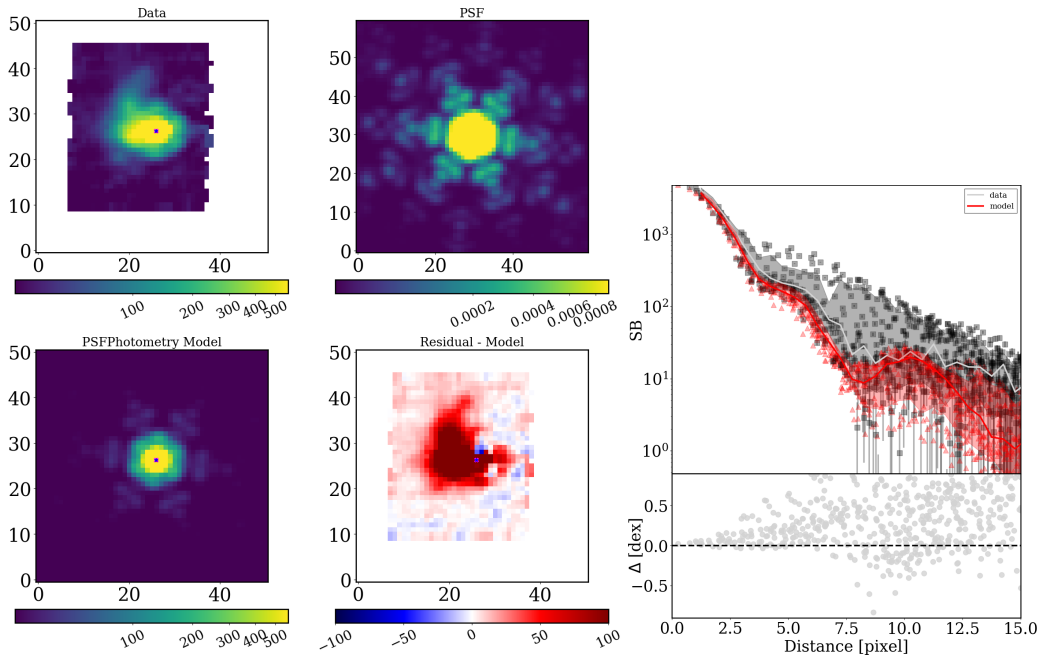


**Figure 11.** Left panels: images from one of the original Channel 3C slices capturing part of the [Ne III] line point-like and extended emission, with corresponding WebbPSF model, best-fit model and final residuals. The blue star indicates the position where the PSF model is centred and then subtracted. The images have the orientation “*ifualign*” and north is to the left. Right panel: radial distribution of the observed data (black), best-fit model (in red) and residuals (gray dots, bottom panel) in the Channel 3C slice shown above. The lack of PSF structure in the residual map and the good match between the radial distributions within  $\sim 3$  px from the point source (Channel 3C PSF FWHM  $\sim 0.6'' \sim 3$  px) validate our point-source subtraction procedure.

Fig. 12 shows the ratio between the original and the PSF subtracted emission-line maps, to highlight which regions and emission lines are mainly affected by the contribution of the point source (darker red). The fitted emission lines are shown in order of their

<sup>4</sup> [https://webbpsf.readthedocs.io/en/latest/jwst\\_ifu\\_datacubes.html](https://webbpsf.readthedocs.io/en/latest/jwst_ifu_datacubes.html)

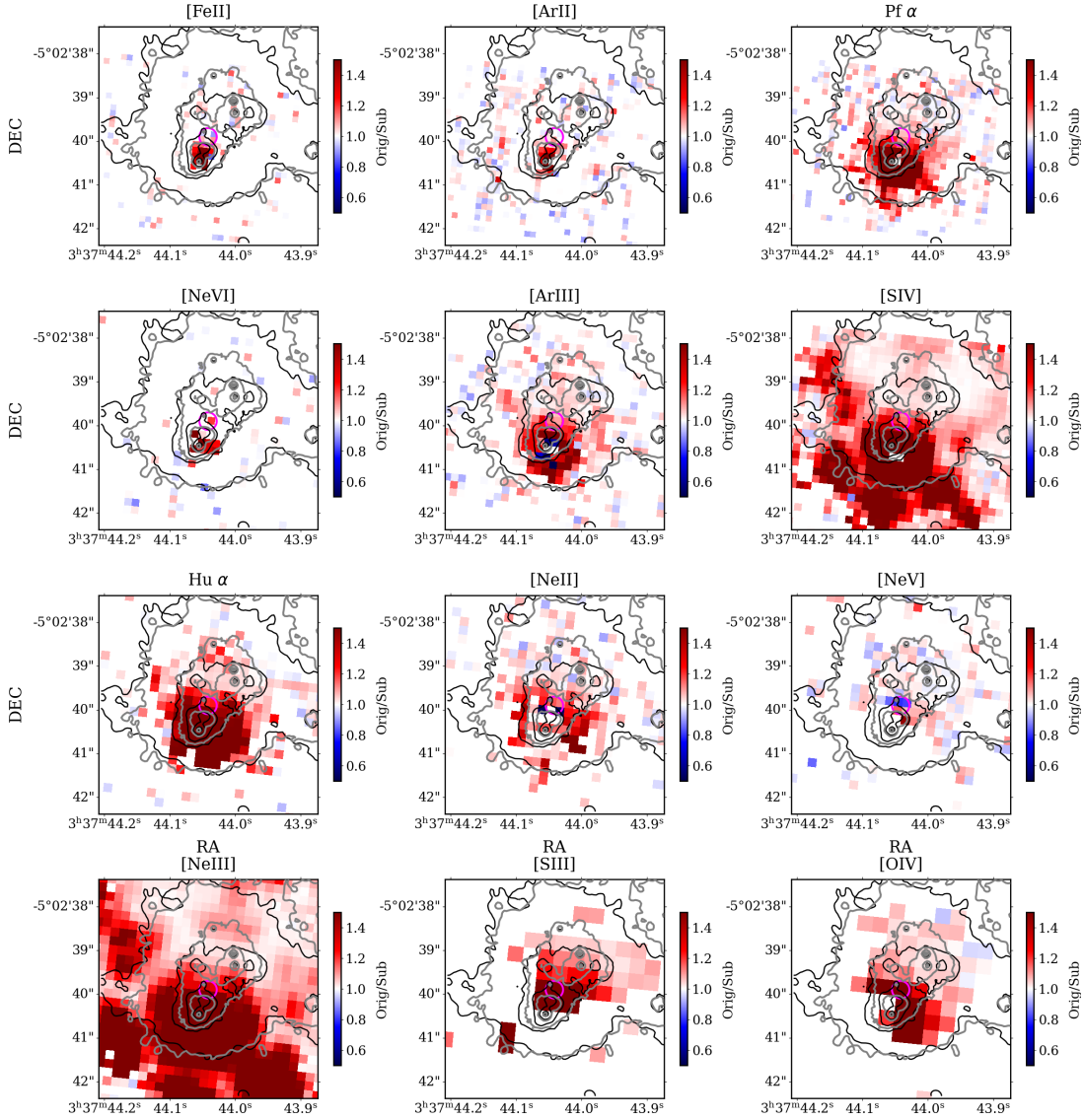


**Figure 12.** Ratio of the original and point-source subtracted maps, highlighting the region dominated by the point source (darker red). All the spaxels with  $S/N > 3$  are shown. [Ne III] and [S IV] are the brightest emission lines observed and show clearly the MIRI/MRS PSF structure. The black and gray contours show the  $H\alpha$  and UV emission, while the magenta circle shows the position of the ULX identified in this galaxy, as shown in Fig. 1. North is up, east is to the left.

wavelength (see Tab. 1). Overall, the point source emission seems to be located in SSC1, as we discuss in Sec. 5.1 (see also Fig. 1).

We applied the same point-source subtraction procedure on the nine band datacubes (A, B, C) of Channel 1, 2 and 3, to retrieve the point-source subtracted spectra for the extended emission continuum and the point source continuum. We used these data to model the continuum with CAFE and estimate the dust attenuation, as explained in Sec. 3.2.

## B. OTHER MIR DIAGNOSTIC DIAGRAMS

In this section we show the [Ne III]/[Ne II] vs [S IV]/[Ne II], color-coded as a function of [O IV]/[Ne III] (Fig. 13) and [Ne III]/[Ne II] versus [O IV]/[Ne III], color-coded as a function of [Ne V]/[Ne II] (Fig. 14), discussed in Sec. 4.4. In the figures, we show the same grids shown in Fig. 8, apart from in Fig. 14 where we also show the R22 disk-plaw models (gray scale) that can reach slightly higher [O IV]/[Ne III]. We comment in detail these figures in Sec. 4.4 and Sec. 5.

We highlight that Fig. 13 diagnostic diagram can be affected by dust attenuation since the [S IV] line lies in the deepest part of the silicate feature (highlighted in grey in Fig. 2, Fig. 3 and Fig. 4). We applied a dust reddening correction (Sec. 3.2) that makes the  $\log([S\ IV]/[Ne\ II])$  line ratio  $\sim 0.1$  dex higher. Also, this diagram is unable to well-separate the low/intermediate and high-ionization emission, given that [S IV] and [Ne III] have similar I.P. and behave similarly. However, it allows us to compare with models also the regions of SBS 0335-052 E with no [Ne V] or [O IV] emission, that are not shown in Fig. 8 and Fig. 14. The magenta line shown in Fig. 13 reports the empirical relation found by Groves et al. (2008), valid - with some scatter - for very different galaxies, including starbursts, ultra-luminous infrared galaxies, AGN, and also BCDs. Interestingly, SSP and SXPs models seem able to replicate the magenta line only at the highest [S IV]/[Ne II], while shocks can only account for the lowest [S IV]/[Ne II] and [Ne III]/[Ne II]. This means that according to the explored set of models, many BCDs could be reproduced only with IMBH models, as shown for SBS 0335-052 E.

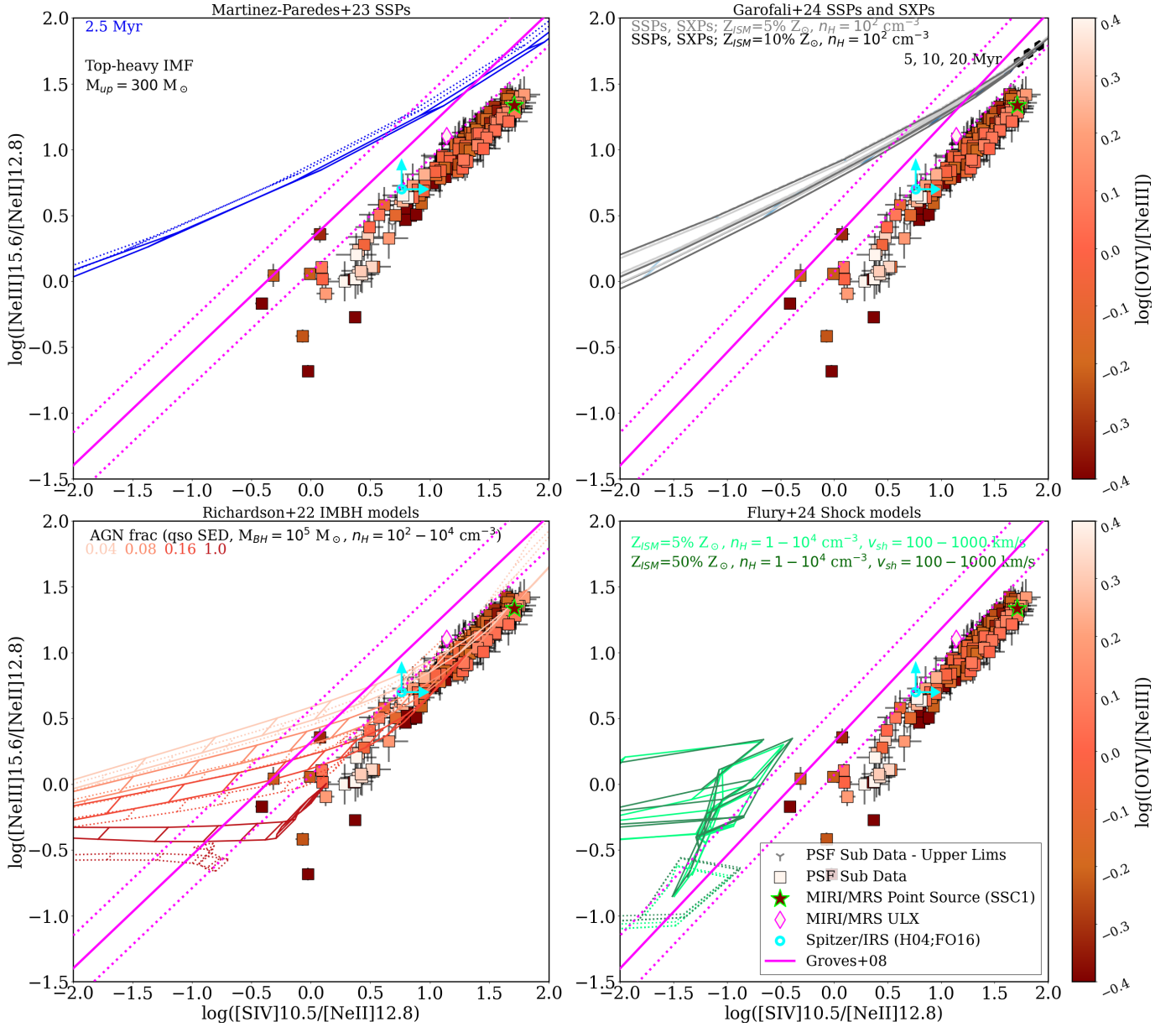
Fig. 14 diagnostic diagram can be more affected by the wavelength-dependent MIRI/MRS PSF and residual fringing than Fig. 8 and Fig. 13, given that [Ne III] lies in Channel 3C and [O IV] in Channel 4C. The effect of the PSF is also probably affecting the ULX [O IV]/[Ne III] (magenta diamond), obtained by fitting the ULX spectrum extracted with a variable (PSF-dependent) aperture (see Sec. 3.1). Indeed, the ULX [O IV]/[Ne III] looks  $\sim 0.5$  dex higher than the median value of the spatially resolved data. R22 IMBH low-density models with a low AGN fraction ( $< 16\%$ ) and partially overlap with the data, but are not able to explain the highest [O IV]/[Ne III] ratios. Young massive stars may be able to explain the point-source (star symbol) line ratios but struggle to reproduce its [Ne V]/[Ne II] upper limit as well as its [S IV]/[Ne II] vs [Ne III]/[Ne II] line ratios shown in Fig. 13.

### C. THE OPTICAL COUNTERPARTS

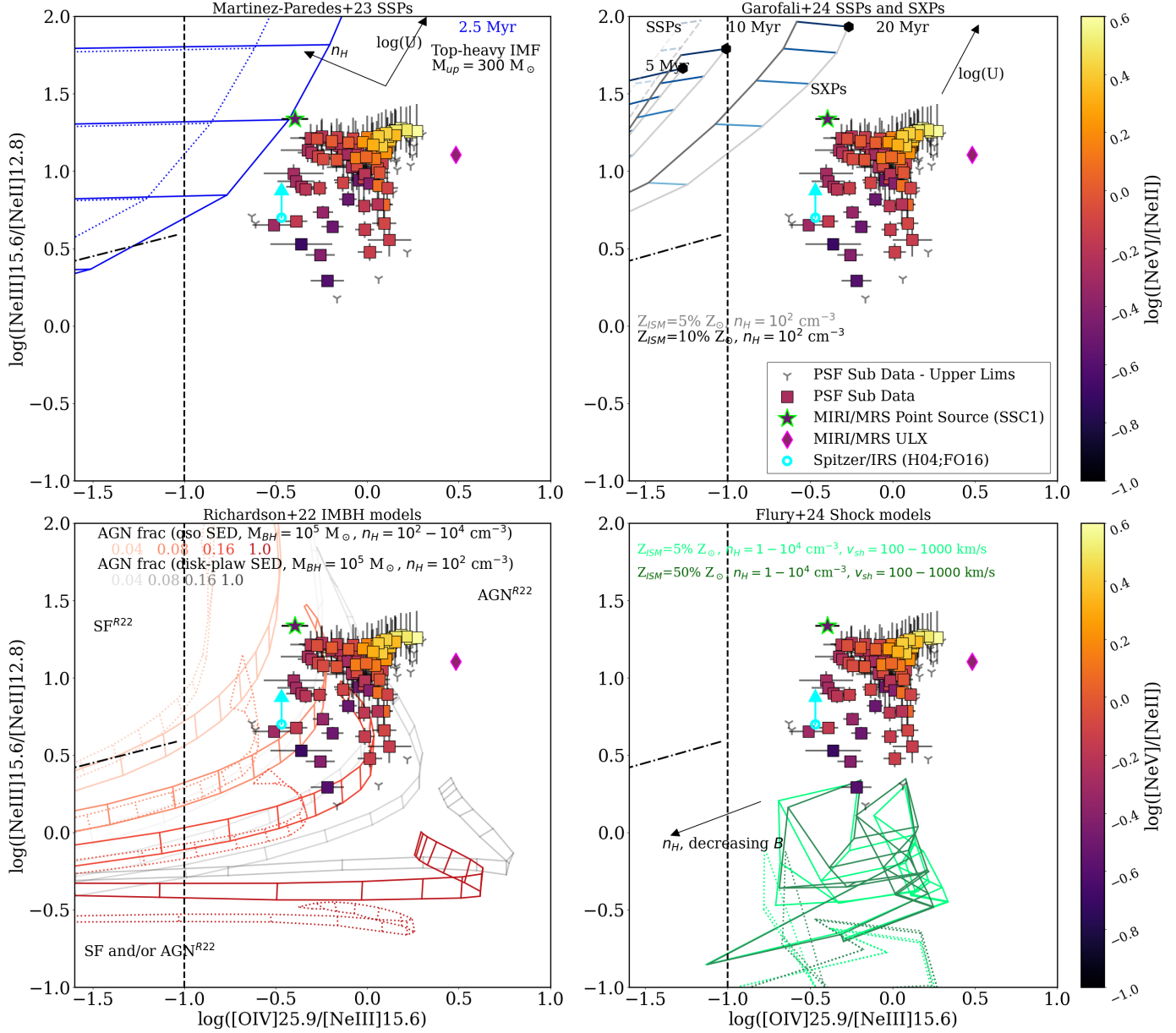
Fig. 15 top panel shows the region around the MIRI/MRS point-source (near SSCs1-2; in black) and the UV and [Ne V] emitting region (around SSCs4-5; in gray) spectra extracted from the MUSE data (ID 096.B-0690A; PI Hayes), with a 3 px ( $\sim 0.6''$ ) extraction radius at the peak of the  $H\alpha$  and He II  $\lambda 4686$  emission, respectively. Consistently with our MIRI/MRS findings, the black spectrum has a larger dust attenuation than the gray one, looking at the different continuum slopes. Interestingly, the  $H\alpha$  line shows a broad profile in both spectra. This is more evident in the black spectrum, which shows also a broad (fainter)  $H\beta$  and [O III]  $\lambda\lambda 5007$ .

Fig. 15 bottom panels show a zoom around the  $H\beta$  and [O III]  $\lambda\lambda 4959, 5007$  (left) and  $H\alpha$  and [Ne II]  $\lambda\lambda 6548, 84$  (right) emission lines, with our best-fit shown in red and blue. To reproduce the black and spectra  $H\alpha$  profiles we added up to 4 Gaussian components, with maximum widths of  $FWHM \sim 1200$  km/s and  $FWHM \sim 400$  km/s, respectively. To fit the forbidden [O III]  $\lambda$  line we added up to 3 Gaussian components, with maximum widths of  $FWHM \sim 900$  km/s and  $FWHM \sim 500$  km/s, respectively.

The full modeling and understanding of the complex kinematics highlighted in the MUSE datacube are beyond the scope of this paper. However, the need for (even broad) multiple Gaussian components in spectra located in different parts of the galaxy and in both permitted and forbidden lines indicates that there is no BH broad line region.



**Figure 13.**  $[\text{Ne III}]/[\text{Ne II}]$  vs  $[\text{S IV}]/[\text{Ne II}]$  diagnostic diagram color-coded as a function of  $[\text{O IV}]/[\text{Ne III}]$  line ratio, with overplotted the same four sets of models of Fig. 8 (higher density models are shown as dotted lines). This diagram allows us to compare with models also the regions of SBS 0335-052 E with no  $[\text{Ne V}]$  or  $[\text{O IV}]$  emission, that are not shown in Fig. 8 and Fig. 14. Clearly, all the models but R22 IMBH (with  $n_{\text{H}} = 100 \text{ cm}^{-3}$ ) struggle to reproduce the displayed line ratios. Our dust attenuation correction made  $\log([\text{S IV}]/[\text{Ne II}])$  line ratio  $\sim 0.1$  dex higher than the observed value.



**Figure 14.**  $[\text{Ne III}]/[\text{Ne II}]$  versus  $[\text{O IV}]/[\text{Ne III}]$  diagnostic diagram color-coded as a function of  $[\text{Ne V}]/[\text{Ne II}]$  line ratio, with overplotted the same four sets of models of Fig. 8. The separators are taken from R22. R22 IMBH low-density models with a low AGN fraction ( $< 16\%$ ) partially overlap with the data, but are not able to explain the highest  $[\text{O IV}]/[\text{Ne III}]$  ratios (the disk-plaw SED can reproduce higher  $[\text{O IV}]/[\text{Ne III}]$  than the qso SED). Young massive stars could explain the point-source (star symbol) line ratios, but struggle to reproduce  $[\text{Ne V}]/[\text{Ne II}]$  upper limit. This diagnostic diagram can be affected by the wavelength-dependent MIRI/MRS PSF and residual fringing, given that  $[\text{Ne III}]$  lies in Channel 3C and  $[\text{O IV}]$  in Channel 4C.

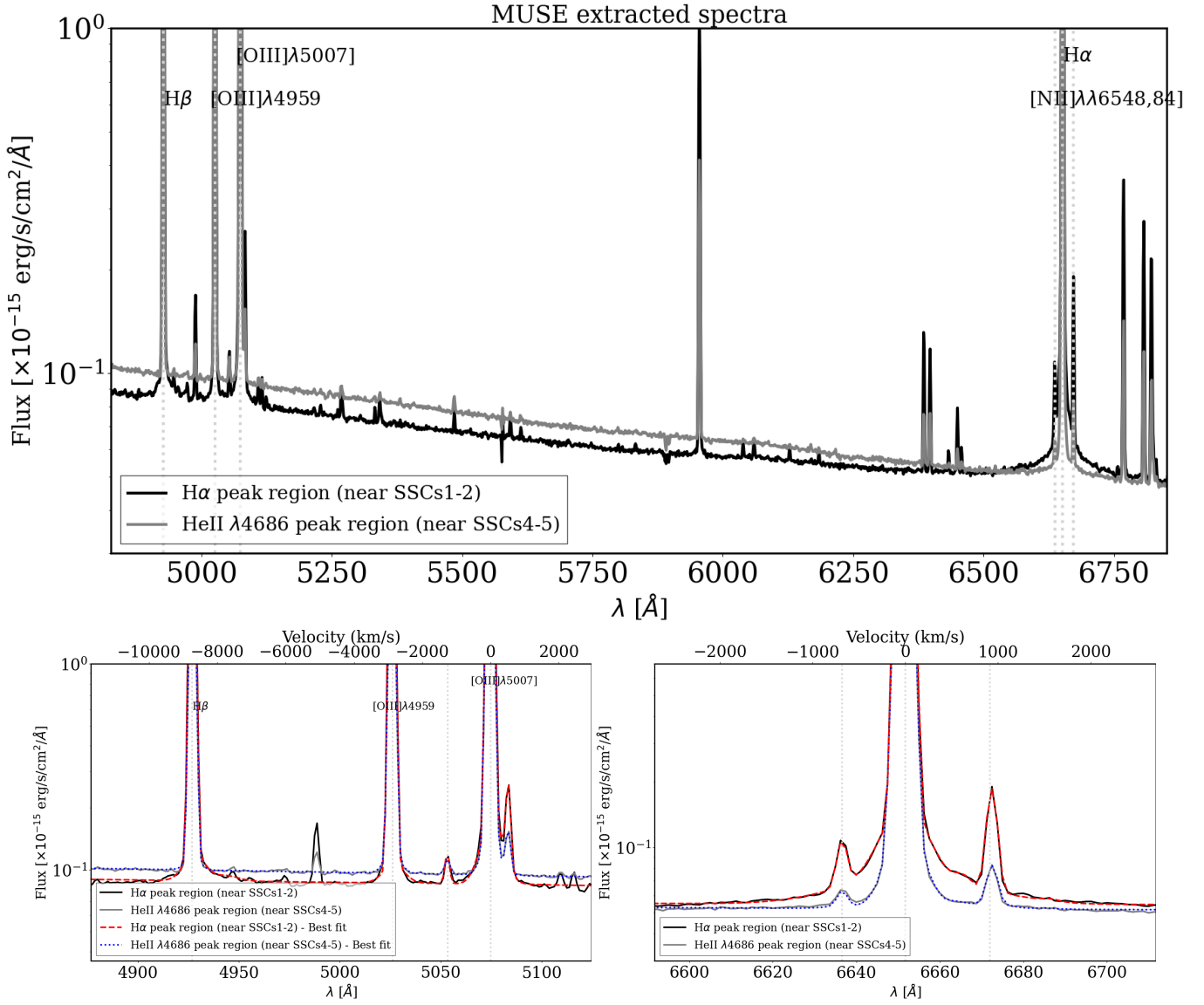


**Figure 15.** Upper panel: Spectra from the point-source region (SSC1; black) and the UV and [Ne V] emitting region (around SSC4+5; gray) from the MUSE data, with a 3-px extraction radius. Bottom panels: Zoom on the H $\beta$ + [O III]  $\lambda\lambda$ 4959,5007 (left) and H $\alpha$ + [N II]  $\lambda\lambda$ 6548,84 (right). Both spectra show a broad H $\alpha$  line that is more visible in the black spectrum, which shows also a (fainter) broad component under H $\beta$  and the forbidden [O III]  $\lambda$ 5007 emission lines, as reported in App. C. This indicates complex kinematics but does not imply the presence of a broad line region.